

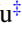


**Quantum statistics engineering in a hybrid nanoparticle-emitter-cavity system**Shuting Shen <sup>\*</sup>, Jiahua Li <sup>†</sup>, and Ying Wu <sup>‡</sup>*School of Physics, Huazhong University of Science and Technology, Wuhan 430074, People's Republic of China* (Received 4 December 2021; revised 17 March 2022; accepted 23 May 2022; published 2 June 2022)

Quantum engineering of photons is a key requirement for the development of quantum technology. Here, we put forward a scheme to investigate extensively quantum statistical characteristics of the photons and their engineering in a hybrid nanoparticle-emitter-cavity architecture through placing a nanoparticle (NP) and a quantum emitter (QE), called NP-QE molecule, into an optical cavity, where the coherent tripartite coupling emerges in the interactions among the NP, QE, and cavity. The photons are collected from the two different channels, i.e., the cavity emission and the NP-QE molecule scattering. Due to the composite nature of the tripartite dressed excitations of our fully coupled system and the destructive interference between different transition pathways for the two-photon excitation, the nontrivial quantum statistical properties, such as unconventional single-photon blockade and strong photon superbunching, can be achieved even within the bad cavity limit (without the need of the strong-coupling condition) when the NP-QE molecule is driven by an external laser not interacting the cavity mode. It is also revealed that the photon autocorrelation and cross-correlation properties are well modified by regulating the size-dependent system parameters, such as the NP-to-QE distance and the NP radius. The small-coupling strength required, the ease of parameter tuning, the relaxation of high-cavity quality factor, and the robustness to the dephasing rate in realistic scenarios all benefit the generation of single-photon sources, which has potential applications in quantum information and quantum communication.

DOI: [10.1103/PhysRevA.105.063702](https://doi.org/10.1103/PhysRevA.105.063702)**I. INTRODUCTION**

As a cornerstone of quantum optics, the study of light-matter interaction has seen tremendous development in the past few decades, which possesses a wide array of applications in various fields such as optical sensing, quantum technologies, and quantum information processing [1]. In general, the interaction between single quantum emitters (QEs), such as single atoms, ions, color centers, molecules, or quantum dots (QDs), and their electromagnetic environment only modifies the spontaneous emission [2]. But, when the coupling is strong enough, the energy levels of the hybrid system are altered, being very different from that of each component, which is crucial for many applications including single-photon source that is an essential ingredient of quantum physics and can satisfy the demands of quantum information and quantum communication [3].

Perfect single-photon source emits only one photon at a time so that the emitted photons exhibit strong antibunching effect, also called photon blockade [4]. Photon blockade effect is considered to be a significant mechanism for generating single-photon source, which is manifested as the strong interaction, leading to the optical response of the subsequent photons obviously modulated by the first one [5–7]. The photon blockade effect under the condition of strong

nonlinear interaction is usually called conventional photon blockade effect, and the physical mechanism behind it is due to the unevenly spaced energy levels of the strongly coupled system comprising an optical or plasmonic cavity and another nonlinear degree of freedom. There have been several proposals for achieving conventional photon blockade effect in cavity quantum electrodynamics (CQED) systems [4,8–11], in circuit CQED systems [12,13], in quantum optomechanical systems [14–16], in second-order nonlinear microcavities [17,18], and in localized surface plasmonic systems [19], etc., just to mention a few.

For conventional photon blockade effect, the strong nonlinear interaction is one of the necessary prerequisites, which makes it the most significant constraint for the implementation of strong antibunching effect for the reason that either the Kerr nonlinearity of the cavity or the coupling rate of the QE cavity must far exceed the system dissipation [5,20]. However, it is well known that it is not easy to realize strong nonlinearity.

In order to eliminate the barrier to strong nonlinearity, Liew and Savona proposed a new mechanism to generate photon blockade in weak nonlinearity [21]. To distinguish the mechanism from the former, it is called unconventional photon blockade effect, whose feature can be understood in terms of destructive quantum interference between different excitation pathways [22]. Based on this mechanism, a variety of systems are proposed to realize the unconventional photon blockade effect, such as CQED systems [20,23–26], coupled superconducting circuit resonators [27], coupled optomechanical systems [28–30], coupled cavities with second- or third-order optical nonlinearity [31–37], and so on.

Due to the large-scale mismatch between light and single emitters, the interaction between them is inherently

<sup>\*</sup>shenst1995@163.com<sup>†</sup>Author to whom correspondence should be addressed: hua-jia\_li@163.com<sup>‡</sup>yingwu2@126.com

weak [38]. To create a light-matter interface customizing the coupling between QEs and photons, two strategies have been developed. One common strategy to remedy this mismatch is to take advantage of CQED [39,40]. When a single QE is placed in a high-finesse cavity, such as Fabry-Perot cavity, micropillar cavity, microring cavity, photonic crystal (PhC) cavity, or superconducting microwave cavity, the photons bounce back and forth many times in the cavity, increasing the opportunity of interaction with QE [41].

Another alternative strategy is to make use of nanoparticles (NPs), a new platform exploring the interaction of light with matter at the nanoscale. Among them, metal NPs have the attractive optical property of enhancing and focusing the light field at the nanoscale, which makes it possible to confine the light field to the subwavelength scale by electromagnetic mode [42]. This capability stems from the fact that metal NPs can support localized surface plasmons (LSPs) (i.e., collective electron oscillations on the metal NP surface) [43,44], which are tightly confined spatially and not limited by diffraction. In addition, in dielectric NPs with high refractive index, optically induced Mie resonances can also supply near-field resonance enhancement [45]. We notice that, based on the LSP advantages, the statistical properties of emitted light from one semiconductor QD interacting with one metal NP, rather than a single-mode dielectric cavity, has been pursued by, for example, considering free-space scattering [46], coupled waveguides [47], and introducing gain media [48] in order to realize nonclassical antibunching effect (sub-Poissonian statistics).

In short, both microcavities and NPs can be used to tailor the light-matter interaction effectively through the Purcell effect, where the cavities usually provide long lifetime of photons (corresponding to high-quality factor  $Q$ ), while the NPs supply enhanced field [49]. Unfortunately, both of them have inevitable disadvantages, that is, the mode volume of the cavity is limited by the diffraction limit, while the metal NPs suffer strong dissipation loss, which limits the occurrence of the better regulation of the interaction between light and matter.

In recent years, some interesting works propose an attractive hybrid NP-QE-cavity configuration by combining the merits of low-loss microcavities with highly localized plasmons, which yields functionalities that exceed those of the individual subunit [50–52]. As illustrated in Refs. [46,53–56], the interplay between the system components is inextricably related to both the size of the components and the distance between them (for example, on the one hand, the NP-QE coupling strength  $g_{me}$  and the NP-cavity interaction coefficient  $g_{cm}$  are closely bound up with the NP radius  $r_m$ ; on the other hand, the NP-QE coupling strength  $g_{me}$  and the QE-cavity interaction coefficient  $g_{ce}$  are closely related to the NP-QE center-to-center distance  $d$ ), resulting in the mutual restriction between the coupling parameters. To our knowledge, the influences of these size-dependent system parameters on the photon-bunching and antibunching properties within the related tripartite system (“NP + QE + cavity”) have not been fully discussed before. Inspired by such a hybrid quantum model and the above progress, in this work we propose a theoretical model of inserting a NP and a QE (also called NP-QE molecule [46]) in an optical cavity, as outlined in Fig. 1, to explore how the size-dependent parameters affect and engineer the statistical properties of both emitted and

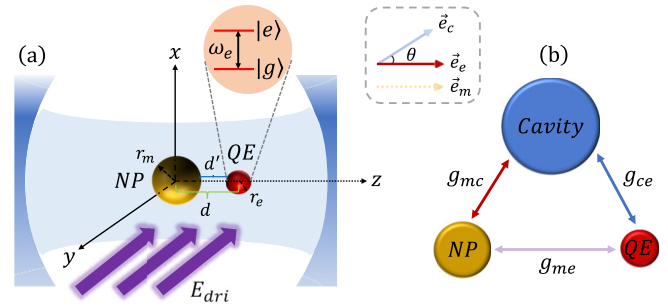


FIG. 1. (a) Schematic picture of the hybrid system composed of a spherical NP and a spherical QE embedded in an optical cavity (not to scale). The NP and QE are separated by a center-to-center distance  $d$ , and both of them are subject to a free-space transverse laser  $E_{dri}$  propagating along the  $y$  direction. Inset: the QE is modeled as a two-level quantum system with the excited state  $|e\rangle$  and the ground state  $|g\rangle$  by considering optical process that interplays with the dipole-allowed transition, where  $\omega_e$  represents the dipole transition frequency of the QE. Here, the QE can be exciton states of single colloidal QD (see Sec. III later for a detailed description), also including PhC cavity and silver NP. In the hybrid NP-QE molecule, there is no direct tunneling interaction between the NP and QE. And the coupling between the NP and QE is due to the long-range Coulomb interaction, promoting energy transfer [57,58]. Shown in the gray dotted box is the schematic diagram of the cavity, QE, and NP polarizations,  $\vec{e}_c$  represents the unit polarization direction of the cavity field, where  $\vec{e}_e$  denotes the unit vector of the dipole moment of the QE, and  $\vec{e}_m$  expresses the unit polarization direction of electric field induced by the NP, respectively. The quantum natures of both the photons emitted by the cavity to guided waveguide (in plane) and the photons scattered by the NP-QE molecule to free space (out of plane) can be measured by the Hanbury Brown–Twiss setup consisting of a beam splitter and two detectors, not shown here. (b) A sketch describing the tripartite interaction among the NP, QE, and cavity where  $g_{mc}$  represents the coupling strength between the NP and cavity,  $g_{ce}$  describes the coupling strength between the QE and cavity, and  $g_{me}$  denotes the coupling strength between the NP and QE. The other symbols are defined and explained in the main text.

scattered photons from this hybrid NP-QE-cavity coupling architecture.

Under the excitation of an external driving field, the occurrences of the NP-QE interaction, the cavity-QE interaction, and the NP-cavity interaction can enrich quantum statistical line shapes of the tripartite hybrid system, as expected. To this end, we analytically and numerically calculate the autocorrelation function of (i) the emitted photons from the cavity, (ii) the scattered photons from the driven NP-QE molecule, and (iii) the cross-correlation function between the cavity emission and the NP-QE scattering, respectively. As a figure of merit, in this work our attention is focused on the dependence of the photon statistics on the size-dependent system parameters, specializing the general framework to realistic experimental scenarios.

Compared with the traditional CQED system containing a single QE, the introduction of the NP can make the system break through the limitation of strong coupling, and make the system obtain the enhanced antibunching or reciprocal transformation from strong antibunching to strong

(super)bunching as well as nonclassical to classical behavior in the weak-coupling scenarios thanks to the composite nature of tripartite excitations. Specifically, the statistical properties of the cavity emission and NP-QE scattering photons have a controllable flexibility by tuning the NP-to-QE distance  $d$  and the NP radius  $r_m$  properly, where the photon statistics can be transformed between antibunched, bunched, or Poissonian. Both the emitted photons from cavity and the scattered photons from NP-QE all characterized by high intensity and strong antibunching can be prepared under the weak-coupling condition in our tripartite hybrid system. For many applications, optical cavities with lower quality factors are preferred owing to the increased spectral width of the cavity mode. In our proposed scheme, photon blockade can be implemented even at very low-quality factor because of the maintenance of antibunching characteristics in a wide range of cavity quality factor, to a certain extent which eliminates the difficulty of experimental implementation. Our model also supports a scheme to achieve single-photon sources with the robustness against the dephasing rate of the QE. Besides, the cross correlation between the cavity emission photons and the NP-QE scattering photons can be shown as anticorrelated or correlated by manipulating the NP-to-QE distance  $d$  or the NP radius  $r_m$ .

The organization of this paper is as follows. In Sec. II, the theoretical model of the tripartite hybrid system under consideration is yielded at the beginning (Sec. II A). The quantum master equation governing the dynamics of the system and the second-order correlation function providing the information of photon statistics are subsequently introduced (Sec. II B). In Sec. III, we elucidate the feasibility of the experiment and introduce the choice of system parameters in detail. In Sec. IV, an analytical discussion for the second-order correlation function of the system is carried out via the Schrödinger equation approach under weak driving-field circumstances. In Sec. V, to begin with, we present the numerical results and compare them with analytical results. After this, the dependence of the statistical properties of the cavity emission photons on various system parameters is investigated via the second-order autocorrelation function numerically in Sec. V A. Second, the photon statistics of the NP-QE scattering photons varying with the size-related parameters are displayed in Sec. V B. Finally, the second-order cross-correlation function  $g_{cp}^{(2)}(0)$  between the cavity emission light and the NP-QE scattering light is investigated in Sec. V C, and the corresponding results show that both anticorrelated and correlated cavity emission photons and NP-QE scattering photons can be generated in our tripartite hybrid system. Conclusions are finally presented in Sec. VI.

## II. BASIC FRAMEWORK OF SYSTEM

### A. Theoretical model and Hamiltonian

As depicted schematically in Fig. 1(a), the hybrid system under consideration is composed of an optical cavity containing a two-level QE and a spherical nonmagnetic NP. The spherical QE with radius  $r_e$  is assembled near the surface of the spherical NP with radius  $r_m$  and frequency-dependent permeability  $\epsilon_m(\omega)$ , and the whole is placed in an optical

cavity. The separation distance between the NP and QE is  $d$  ( $d - r_m - r_e > 2$  nm) [46], which ensures there is no direct tunneling between them. The NP and QE are excited by an external applied driving field  $E_{\text{dri}} = E_0 e^{-i\omega_d t} + \text{c.c.}$ ,  $E_0$  being the amplitude,  $\omega_d$  being the angular frequency, and c.c. denoting the complex conjugation. The propagation direction of the driving field  $E_{\text{dri}}$  is along the  $y$  axis, and its polarization direction is set to be parallel or perpendicular to the axis joining the NP and QE structures.

When light is applied to a NP whose size is smaller than or comparable to the skin depth (for noble metal gold or silver, the skin depth is about 25 nm), the external light field can penetrate the entire dielectric sphere and drive the collective wavelike motion of free electrons on the NP surface [59]. Further, if the frequency of excitation light is close to the resonance frequency of plasmonic mode, the nonpropagating localized surface plasmons resonance (LSPR) occurs, which enables the NP to maintain the electromagnetic field energy in the form of electromechanical energy, giving rise to light field enhancement and concentration at the nanoscale.

At the same time, the precondition that the size of the NPs is much smaller than the wavelength of incident light allows that the external light field which is applied to the NPs can be regarded as uniform and in phase. Furthermore, when considering the NP-QE molecule, the size of components and the distance between them are considered small enough such that the retardation effects can be ignored conveniently, which further demonstrates the validity and rationality of using quasistatic approximation to describe the scattering of the NPs [60,61]. Besides, it is natural to use the dipole approximation to describe the properties of individual subwavelength NPs, and the dipole approximation is still valid when the NP-QE distance is large relative to the size of components [62,63].

When the electric field is applied to the hybrid NP-QE, the oscillating electric field not only excites the NP mode, but also couples the QE transition [64]. The superposition field sensed by the NP is composed of the external driving field and the additional field generated by the oscillating dipole moment caused by the dipole transition of the QE. At the same time, the dipole transition of the QE also feels the influence of the NP mode correspondingly, thus forming self-feedback. The excitation field polarizes the NP-QE molecule, thus leading to a dipole-dipole coupling between them.

Under the dipole and rotating-wave approximations, the Hamiltonian of the whole quantum system describing the NP-QE-cavity coupling process can be written as

$$\hat{H}_{\text{tot}} = \hat{H}_0 + \hat{H}_{\text{int}} + \hat{H}_{\text{dri}}, \quad (1)$$

where each term will be explained in detail below.

The first term  $\hat{H}_0$  on the right-hand side (RHS) of Eq. (1), associated with the free-energy Hamiltonian of the isolated cavity, NP, and QE, can be represented as

$$\hat{H}_0 = \hbar\omega_c \hat{c}^\dagger \hat{c} + \hbar\omega_m \hat{m}^\dagger \hat{m} + \hbar\omega_e \hat{\sigma}^\dagger \hat{\sigma}, \quad (2)$$

where  $\hbar$  is the reduced Planck's constant.  $\omega_c$  is the resonance frequency of the cavity field,  $\hat{c}^\dagger$  and  $\hat{c}$  denote the photon creation and annihilation operators for the cavity mode, respectively, fulfilling the usual bosonic commutation relation  $[\hat{c}, \hat{c}^\dagger] = 1$ . The dielectric function of the NP can be characterized by a frequency-dependent Drude model  $\epsilon_m(\omega) =$

$\epsilon_\infty - \omega_p^2/(\omega^2 + ik_m\omega)$  [44,46]. Here,  $\epsilon_\infty$  is the ultraviolet permittivity of metal,  $\omega_p$  is the plasma frequency, and  $\kappa_m$  is the damping rate of metal, respectively. In light of the Drude model and making use of the Fröhlich condition  $\text{Re}[\epsilon_m(\omega)] = -2\epsilon_b$  [44] with  $\text{Re}[\cdot]$  referring to the real part of the magnitude enclosed in square brackets, it can be deduced that the resonant frequency  $\omega_m$  of the NP plasmonic field mode is  $\omega_m = \omega_p/\sqrt{2\epsilon_b + \epsilon_\infty}$ , with  $\epsilon_b$  being the relative permittivity of the environment where the NP-QE molecule is embedded.  $\hat{m}^\dagger$  and  $\hat{m}$  are the bosonic creation and annihilation operators describing the NP plasmonic field mode. For convenience, we have taken the zero-point energies for the NP and cavity fields to be the zeros of energies since they only yield a relative shift and do not affect the system dynamics. As shown in Fig. 1(a), the QE can be modeled as a two-level system with a ground state  $|g\rangle$ , an excited state  $|e\rangle$ , and a dipole-allowed transition frequency  $\omega_e$ , respectively. The energy of the ground state  $|g\rangle$  is set as zero for the sake of simplicity.  $\hat{\sigma} = |g\rangle\langle e|$  and its conjugate operator  $\hat{\sigma}^\dagger = |e\rangle\langle g|$  represent the ladder operators of the QE, satisfying the fermionic anticommutation relations  $\{\hat{\sigma}^\dagger, \hat{\sigma}\} = 1$ .

The second term  $\hat{H}_{\text{int}}$  on the RHS of Eq. (1), associated with the dipole-dipole interaction Hamiltonian between the NP and QE, the QE-cavity interaction Hamiltonian between the QE and cavity, and the NP-cavity interaction Hamiltonian between the NP and cavity [see Fig. 1(b)], can be expressed as

$$\begin{aligned} \hat{H}_{\text{int}} = & i\hbar g_{me}(\hat{m}^\dagger \hat{\sigma} - \hat{m} \hat{\sigma}^\dagger) + i\hbar g_{ce}(\hat{c}^\dagger \hat{\sigma} - \hat{c} \hat{\sigma}^\dagger) \\ & + \hbar g_{mc}(\hat{m}^\dagger \hat{c} + \hat{m} \hat{c}^\dagger), \end{aligned} \quad (3)$$

where  $g_{me}$  characterizes the degree of dipole-dipole coupling between the NP mode and the QE, with the form of  $g_{me} = \vec{\mu} \cdot \vec{e}_m(S_\alpha/d^3)\sqrt{3\eta r_m^3/(4\pi\hbar\epsilon_0)}$ . Details of the derivation are given in Refs. [56,65]. Here,  $\vec{\mu} = \mu\vec{e}_e$  is the dipole moment of the QE, with  $\mu$  representing the magnitude of the dipole moment of the QE (assuming that  $\mu$  is real without loss of generality, i.e.,  $\mu^* = \mu$ ) and  $\vec{e}_e$  being the unit vector of the dipole moment of the QE, and  $\vec{e}_m$  is the unit polarization direction of the dipole response field created by the NP. Since we consider that the dipole moment of the QE is aligned with that of the electric field caused by the NP, the coupling strength  $g_{me}$  can be written as the form of  $g_{me} = \mu(S_\alpha/d^3)\sqrt{3\eta r_m^3/(4\pi\hbar\epsilon_0)}$  [46]. Here,  $S_\alpha$  is the orientation parameter, with  $S_\alpha = 2$  ( $S_\alpha = -1$ ) for the polarization of the external driving field being parallel (orthogonal) to the axis joining the NP and QE structures.  $\eta$  is defined as  $\eta = \{d \text{Re}[\epsilon_m(\omega)]/d\omega|_{\omega=\omega_m}\}^{-1} = [\kappa_m^2(2\epsilon_b + \epsilon_\infty) + \omega_p^2]/[2(2\epsilon_b + \epsilon_\infty)^{3/2}\omega_p^3]$  [65], and  $\epsilon_0$  is the vacuum permittivity.

Before continuing, we would like to add a few remarks. The metal NP has the attractive optical property that can support the LSPs, enabling it to enhance optical fields both inside and in the near-field zone outside the NP [44]. In this work, we only focus on the electric field outside the NP (i.e.,  $d > r_m + r_e$ ). Under the excitation of the external driving field  $E_{\text{dri}}$ , the NP will react to the superposition field composed of the external driving field and the dipole response field of the QE, thus generating an electric field in the form of  $E_m = S_\alpha P_{np}/(4\pi\epsilon_0\epsilon_b d^3)$  outside the NP [46,55,56].

Here,  $P_{np} = 4\pi\epsilon_0\epsilon_b\beta r_m^3[E_0 + S_\alpha P_{\text{QE}}/(4\pi\epsilon_0\epsilon_b d^3)]$  denotes the dipole moment of the NP,  $\beta = [\epsilon_m(\omega) - \epsilon_b]/[\epsilon_m(\omega) + 2\epsilon_b]$  is the Clausius-Mossotti factor of the NP, and  $P_{\text{QE}}$  represents the dipole moment of the QE, respectively. The above expressions convey an obvious message: the NP dipole response field is positively correlated with the size of the NP. With the aid of CQED methods, the optical field of the NP can be quantized, and then the dipole-dipole coupling strength  $g_{me} = \mu(S_\alpha/d^3)\sqrt{3\eta r_m^3/(4\pi\hbar\epsilon_0)}$  between the NP and the QE can be derived accordingly [46,54–56]. The coupling strength between the NP and the QE placed near the surface of the NP is proportional to the effective mode volume of the NP, which is different with the usual Jaynes-Cummings coupling form of the QE embedded into optical cavity [53] or placed on the surface of NP [66], also reminiscent of the result described in [67] (i.e., the cavity-QE coupling is proportional to  $1/\sqrt{V}$ ,  $V$  is the effective volume of the cavity). Physically, the oscillating electric field created by the external driving field  $E_{\text{dri}}$  can generate plasmon oscillations in the NP and electric dipoles in the QE, which interact with each other via the dipole-dipole interaction (Coulomb interaction) and, in turn, renormalize the oscillating electric field. This is the fundamental reason why increasing the NP size  $r_m$  can lead to an increase in the NP-QE coupling strength  $g_{me}$ .

It is demonstrated in Ref. [68] that the metal NP responds basically as an induced dipole for diameters below  $\sim 150$  nm and the higher-multipole modes should be considered at larger sizes. In the following discussion, we consider the case where the size of the NP is much less than 150 nm and the QE is placed at a distance about or above  $2r_m$  from the NP, which is sufficient to ignore the high-order multipole effect as well as the direct tunneling effect.

And then,  $g_{ce}$  indicates the position-dependent coupling coefficient between the QE and cavity mode, taking the form of  $g_{ce} = \vec{\mu} \cdot \vec{e}_c\sqrt{\omega_c/(2\hbar\epsilon_0\epsilon_b V_c)}f(\mathbf{r}_e)$  with  $\vec{e}_c$  representing the unit polarization direction of the cavity field and  $V_c$  being the mode volume of the cavity [50,69]. The relative orientation between the dipole moment of the QE and the polarization vector of the cavity field is denoted by an angle  $\theta$  (as shown in set of Fig. 1), thus, the coupling coefficient between the QE and cavity mode can be further expressed as  $g_{ce} = \mu \cos\theta\sqrt{\omega_c/(2\hbar\epsilon_0\epsilon_b V_c)}f(\mathbf{r}_e)$ . Here,  $f(\mathbf{r}) = f(x, y)f(z)$  is the normalized mode distribution function describing the distribution of cavity field, where  $f(x, y)$  denotes the transverse spatial mode profile and maximizes when the coordinates  $(x, y)$  take  $(0, 0)$ , i.e.,  $f(x, y)|_{x=0, y=0} = 1$ , whereas  $f(z) = \cos(2\pi z/\lambda_c)$  represents the longitudinal spatial mode function with  $\lambda_c$  being the resonance wavelength of the cavity mode. As shown in Fig. 1(a), we assume that NP is placed at the origin of the coordinate axis, and the relative position between the NP and QE changes on the  $z$ -coordinate axis, i.e., the position vector  $\mathbf{r}_m$  of the NP is  $(0, 0, 0)$ , and the position vector  $\mathbf{r}_e$  of the QE is  $(0, 0, d)$  taken with respect to the center of the NP. This makes the normalized mode distribution function  $f(\mathbf{r})$  at the location of QE in the form of  $f(\mathbf{r}_e) = f(x, y)|_{x=0, y=0}f(z)|_{z=d} = \cos(2\pi d/\lambda_c)$ .  $g_{mc}$  represents the interaction coupling strength between the NP and cavity modes, which can be further expressed as  $g_{mc} = 2\pi\epsilon_b r_m^3 \cos\theta\sqrt{\omega_m\omega_c/(\epsilon_g\epsilon_b V_m V_c)}f(\mathbf{r}_m)$  [50], with selecting  $f(\mathbf{r}_m) = f(x, y)|_{x=0, y=0}f(z)|_{z=0} = 1$ .

The third term  $\hat{H}_{\text{dri}}$  on the RHS of Eq. (1) referring to the Hamiltonian of the driving of the NP and QE by the external driving field  $E_{\text{dri}}$ , can be written as

$$\begin{aligned} \hat{H}_{\text{dri}} = & -\hbar(\Omega_m \hat{m}^\dagger e^{-i\omega_d t} + \Omega_m^* \hat{m} e^{i\omega_d t}) \\ & -\hbar\Omega_e(\hat{\sigma}^\dagger e^{-i\omega_d t} + \hat{\sigma} e^{i\omega_d t}), \end{aligned} \quad (4)$$

where  $\Omega_m = E_0\chi/\hbar$  and  $\Omega_e = E_0\mu/\hbar$  are, respectively, the Rabi frequencies for the coupling of the external driving laser to the NP mode and the QE, resulting from the dipole interaction of the NP and QE with  $E_{\text{dri}}$  [55,56].  $E_0 = \sqrt{2I_p/(\sqrt{\epsilon_b}\epsilon_0 c)}$  is the amplitude of the external driving laser with  $I_p = \sqrt{\epsilon_b}\epsilon_0 c E_0^2/2}$  being the intensity of the driving laser and  $c$  denoting the vacuum light speed.  $\chi = -i\epsilon_b\sqrt{12\pi\epsilon_0\eta\hbar r_m^3}$  is the dipole moment of the NP [65]. Thus,  $\Omega_m$  and  $\Omega_e$  can be further represented as  $\Omega_m = -i\epsilon_b\sqrt{24\pi I_p\eta r_m^3}/(\sqrt{\epsilon_b}\hbar c)$  and  $\Omega_e = (\mu/\hbar)\sqrt{2I_p}/(\sqrt{\epsilon_b}\epsilon_0 c)$ , respectively.

For convenience, the system dynamics can be rotated with respect to the driving laser frequency  $\omega_d$  by applying the operator  $\hat{U}(t) = \exp[i\omega_d t(\hat{c}^\dagger\hat{c} + \hat{m}^\dagger\hat{m} + \hat{\sigma}^\dagger\hat{\sigma})]$ , which leads to an effective Hamiltonian  $\hat{H}_{\text{eff}} = \hat{U}\hat{H}_{\text{tot}}\hat{U}^\dagger - i\hbar\hat{U}(d\hat{U}^\dagger/dt)$ , being of the form

$$\begin{aligned} \hat{H}_{\text{eff}} = & \hbar\Delta_c\hat{c}^\dagger\hat{c} + \hbar\Delta_m\hat{m}^\dagger\hat{m} + \hbar\Delta_e\hat{\sigma}^\dagger\hat{\sigma} \\ & + i\hbar g_{me}(\hat{m}^\dagger\hat{\sigma} - \hat{m}\hat{\sigma}^\dagger) + i\hbar g_{ce}(\hat{c}^\dagger\hat{\sigma} - \hat{c}\hat{\sigma}^\dagger) \\ & + \hbar g_{mc}(\hat{m}^\dagger\hat{c} + \hat{m}\hat{c}^\dagger) - \hbar(\Omega_m\hat{m}^\dagger + \Omega_m^*\hat{m}) \\ & - \hbar\Omega_e(\hat{\sigma}^\dagger + \hat{\sigma}), \end{aligned} \quad (5)$$

in which  $\Delta_c = \omega_c - \omega_d$ ,  $\Delta_m = \omega_m - \omega_d$ , and  $\Delta_e = \omega_e - \omega_d$  define the detunings of the cavity mode ( $\omega_c$ ), the NP mode ( $\omega_m$ ), and the QE ( $\omega_e$ ) from the driving field ( $\omega_d$ ), respectively. In particular, if considering the situation of  $g_{me} = g_{mc} = \Omega_m = 0$  (NP decoupled), in other words, the role of the NP is ignored and we only care about the coupled QE-cavity system, Eq. (5) is simplified to the well-known Jaynes-Cummings model [53]. Alternatively, if thinking over another case where  $g_{ce} = g_{mc} = 0$  (cavity decoupled), the above Hamiltonian characterizes a hybrid NP-QE molecule system which has been studied in detail in Ref. [46]. We refer the reader to Refs. [50,65] for technical details of the derivation about the whole system Hamiltonian.

### B. Master equation and second-order correlation function

In general, there are losses in the cavity and NP-QE molecule, which makes it an open system. To this end, taking the dissipation into account, the dynamics of the hybrid NP-QE-cavity system can be depicted by the Born-Markov quantum master equation:

$$\begin{aligned} \frac{d\hat{\rho}}{dt} = & -\frac{i}{\hbar}[\hat{H}_{\text{eff}}, \hat{\rho}] + \kappa_c\mathcal{D}(\hat{c})\hat{\rho} + \kappa_m\mathcal{D}(\hat{m})\hat{\rho} \\ & + \gamma_s\mathcal{D}(\hat{\sigma})\hat{\rho} + \gamma_d\mathcal{D}(\hat{\sigma}^\dagger\hat{\sigma})\hat{\rho}, \end{aligned} \quad (6)$$

where  $\hat{\rho}$  is the density operator of the fully coupled tripartite system and  $\mathcal{D}(\hat{O})\hat{\rho} = \hat{O}\hat{\rho}\hat{O}^\dagger - 1/2\hat{O}^\dagger\hat{O}\hat{\rho} - 1/2\hat{\rho}\hat{O}^\dagger\hat{O}$  is a general Lindblad operator form for the collapse operator  $\hat{O}$ , answering for the incoherent loss of the system. For the dissipation,  $\kappa_c$  denotes the decay rate of the cavity mode and  $\kappa_m = \kappa_r + \kappa_{nr}$  accounts for the damping rate of the NP plasmonic

field mode, covering both the radiation loss  $\kappa_r$  caused by radiation to the far field and the nonradiation loss  $\kappa_{nr}$  caused by Ohmic loss.  $\gamma_s$  and  $\gamma_d$  represent the spontaneous emission rate and the dephasing rate of the two-level QE, respectively.

The figure of merit quantifying the single-photon degree for this coupled quantum system is the equal-time second-order autocorrelation function, defined as

$$g_A^{(2)}(0) = \frac{\text{Tr}(\rho_{ss}\hat{A}^\dagger\hat{A}^\dagger\hat{A}\hat{A})}{[\text{Tr}(\rho_{ss}\hat{A}^\dagger\hat{A})]^2}, \quad (7)$$

where  $\rho_{ss}$  is the steady-state solution by setting  $d\hat{\rho}/dt = 0$  in Eq. (6). The notation  $\hat{A}$  can be referred to the photon annihilation operator  $\hat{c}$  for the cavity mode, i.e.,  $\hat{A} = \hat{c}$  which corresponds to the photons emitted by the cavity mirror, or the total polarization operator  $\hat{p}$  for the hybrid NP-QE molecule, i.e.,  $\hat{A} = \hat{p} = \chi^*\hat{m} + \mu\hat{\sigma}$  [46,55,56] which corresponds to the photons scattered by the NP-QE molecule in free space. The autocorrelation function  $g_A^{(2)}(0)$  describes the conditional probability for detecting a second photon simultaneously, given that a photon is detected in the same channel. On the other hand, mutual correlations between the cavity emission photons and the NP-QE scattering photons can also be investigated through an equal-time second-order cross-correlation function

$$g_{cp}^{(2)}(0) = \frac{\text{Tr}(\rho_{ss}\hat{c}^\dagger\hat{p}^\dagger\hat{c}\hat{p})}{[\text{Tr}(\rho_{ss}\hat{c}^\dagger\hat{c})\text{Tr}(\rho_{ss}\hat{p}^\dagger\hat{p})]}, \quad (8)$$

where the cross-correlation function  $g_{cp}^{(2)}(0)$  can be interpreted as the modified photon output of one channel conditioned on the presence of a photon in the other channel.

As a significant index, the equal-time second-order intensity correlation function  $g^{(2)}(0)$  can well evaluate the statistical properties of photons. Specifically,  $g^{(2)}(0) < 1$  amounts to sub-Poisson statistics (photon antibunching). Ideally, it indicates the complete photon blockade when  $g^{(2)}(0)$  approaches zero, which can be used to prepare a perfect single-photon source.  $g^{(2)}(0) = 1$  corresponds to Poisson statistics, i.e., a coherent field.  $g^{(2)}(0) > 1$  corresponds to super-Poisson statistics. More detailed division can be distinguished:  $1 < g^{(2)}(0) < 2$  corresponds to photon bunching,  $g^{(2)}(0) = 2$  stands for thermal or chaotic photon, and  $g^{(2)}(0) > 2$  refers to photon superbunching or extra bunching [70].

### III. EXPERIMENTAL FEASIBILITY AND SYSTEM PARAMETER CHOICE

In this section, an assessment of the experimental feasibility of the present scheme is in order. Below we consider, for concreteness, single colloidal QD, metal NP, and PhC cavity as a possible implementation of our proposed tripartite coupling system. Fabrication can be performed via mainly employing chemical synthesis, electron beam lithography, and inductively coupled plasma-etching techniques.

First, colloiddally synthesized QD with emission wavelength tunability and chemical flexibility [71] has a variety of potential applications in optoelectronics including optical amplifiers, lasers, and so on. Inexpensive and scalable wet chemical synthesis procedures can be utilized to chemically synthesize colloidal QDs with sufficiently small sizes (average 1 to 6 nm in radius) [72–74], which has the capability

to furnish routine preparation of semiconductor nanocrystals. Advanced semiconductor synthetic methodology can accurately adjust both the size and shape of colloidal QD with near-atomic-layer precision [73,74]. Current experiments have allowed for preparing and manipulating one, two, and multiple CdSe colloidal QDs [75,76]. In addition, single colloidal CdSe QD with a size of 1 nm and an energy gap of about 2.9 eV has also been reported in experiment [71].

Inspired by these state-of-the-art experiments, the size  $r_e$  of colloidal QD can be designed to be much smaller than the center-to-center distance  $d$  between the QD and NP ( $r_e \ll d$ ), while again  $d$  is much smaller than the wavelength of the incident light  $\lambda$  ( $d \ll \lambda$ ). As a result, within the QD, the electric field induced by the incident light is uniform, and the QD can be modeled as a pointlike dipole emitter. However, for the metal NP coupled to the QD, the dependencies of the electric field on NP's size need to be considered. Alternatively, when colloidal QD is treated quantum mechanically in the form of discrete energy levels, a few degenerate excited levels exist. Here, we approximate the QD as a simplified two-level model. In more realistic calculations beyond the two-level approximation, one has to consider complicating effects, such as the degenerate excited states with different dipole moments, which is left for further study owing to the need to compute large matrices with complex entries.

Second, semiconductor metal NP sample can be prepared by means of advanced electron-beam lithography, seed-mediated growth method, and template-stripping technology [77–79], also which is commercially available. Experimentally, in order to overcome the difficulty of accurately spatial positioning of a single QD within the nanometer range of a metal NP, Hartsfield *et al.* demonstrated the strong QD-NP coupling by controlling a CdSe/ZnS QD (3 nm in radius) near a spherical Au NP (15 nm in radius) through atomic force microscopy (AFM) operation that enables one to carefully tailor the dimensions of an individual structure with a precise positioning of QD with below 5 nm accuracy [80]. Ratchford *et al.* positioned a single Au NP near a CdSe/ZnS QD to construct a hybrid nanostructure with variable geometry using AFM nanomanipulation [81], which promotes the feasibility of our proposed model. More high accuracy for the spatial positioning of QD in experiment in contrast with [80] may be challenging under current technologies, which requires the further development of microfabrication and nanotechnology.

Finally, PhC nanocavity can be fabricated using electron beam lithography, reactive ion etching, and chemical wet etching. The details of the fabrication procedure for realizing such PhC cavities can be found in [82,83]. The resonant frequency of PhC cavity mode can be varied either by xenon gas deposition technique (coarse tuning) [84] or by temperature-tuning technique (fine tuning) [85]. It has been shown that chemically synthesized nanocrystals, such as CdSe, PbS, and PbSe colloidal QDs, can be site selectively inserted on PhC cavity by the means of AFM lithography and surface chemistry techniques, which has checked to be robust that colloidal QDs can be bounded to the target region [86–88]. On the other hand, semiconductor metal NP can be embedded in a PhC cavity using a nanoassembly method that combines a modified dip pen technique with AFM manipulation, which allows the assembly and rearrangement of enough small

plasmonic structures [89–93]. For example, in Ref. [93], Fröch *et al.* demonstrated a feasible solution using PhC slab design and fabrication method for hybrid integration of NP and PhC cavity, which can achieve efficient coupling between components. Although no single experimental QD-NP-cavity setup currently satisfies all the requirements needed for realizing the antibunched statistics under study, this may be remedied in the near future due to increasing advances in nanotechnology.

The quantum nature of the output light can be confirmed by performing a Hanbury Brown–Twiss type experiment [94], which comprises a 50:50 beam splitter with transmittivity  $\frac{1}{2}$  and two single-photon avalanche diodes (SPADs) for the second-order correlation  $g^{(2)}$  measurement, and two beam splitters (the first one with transmittivity  $\frac{2}{3}$  and the other with  $\frac{1}{2}$ ) and three SPADs for the third-order correlation  $g^{(3)}$  measurement. The photons emitted by the PhC cavity can be detected by introducing a PhC waveguide [95,96] in the vicinity of the cavity in the  $x$ - $z$  plane, whereas the out-of-plane photons scattered by the NP-QD molecule can be probed perpendicular to the PhC membrane of the  $x$ - $z$  plane where a pinhole in the detection path is used for spatial filtering of the cavity emission [92].

In order to evaluate our proposed scheme, in the following we consider the specific case of Ag NP as an example, whose frequency-dependent dielectric permittivity can be expressed as  $\epsilon_m(\omega) = \epsilon_\infty - \omega_p^2/(\omega^2 + i\kappa_m\omega)$  [44]. Here, the related material parameters are selected as follows: the ultraviolet permittivity of Ag  $\epsilon_\infty = 5$  [55], the NP bulk plasma frequency of Ag  $\omega_p = 7640.21$  meV (corresponding to the resonant frequency of the Ag NP  $\omega_m = \omega_p/\sqrt{2\epsilon_b + \epsilon_\infty} = 2887.73$  meV in vacuum,  $\epsilon_b = 1$ ), and the damping of Ag  $\kappa_m = 53.28$  meV [46], respectively. The PhC cavity quality factor is calculated to be  $Q = \omega_c/\kappa_c = 10^4$  when taking the cavity resonance frequency  $\omega_c \sim \omega_m$  and the cavity loss  $\kappa_c = 0.2887$  meV. The cavity mode volume is set to  $V_c = 1\mu\text{m}^3$ . These are typical values for the metal NP and PhC cavity systems realized experimentally, with similar behavior expected for a range of parameters. Apart from that, the dipole moment and spontaneous emission rate of the QD are set to  $\mu = 0.7$  nm and  $\gamma_s = 50$   $\mu\text{eV}$  [46], unless otherwise stated. Lastly, a weak driving field  $E_{\text{dri}}$  with intensity  $I_p = \sqrt{\epsilon_b\epsilon_0}cE_0^2/2 = 1\text{W}/\text{cm}^2$  in free space is applied to drive the hybrid NP-QD molecule. The polarization direction of the driving field is set to be parallel to the orientation of the QD dipole moment, where the polarization of the driving field can be controlled via a  $\lambda/2$  wave plate. Note that the NP dipole moment is induced by the driving field and its orientation is consistent with the polarization direction of the driving field. There is an angle  $\theta$  between the direction of the QD dipole moment and the polarization direction of the cavity field.

#### IV. ANALYTICAL SOLUTIONS OF SECOND-ORDER CORRELATION FUNCTION UNDER WEAK-DRIVING CONDITION

In this section, we present here approximately analytical expressions for the system observables as an alternative method to characterize the photon statistical properties of the NP-QE-cavity coupling system. The quantum state can be

indicated as an expansion based on a Fock state basis. Under a weak driving limit, the population of the high-photon excitation states is so low that the total excitation number of the Hilbert space can be truncated to a lower value. Therefore, the wave function of the system can be reasonably approximated in the two-excitation manifold as

$$\begin{aligned}
 |\Psi(t)\rangle = & C_{0,0,g}|0, 0, g\rangle + C_{1,0,g}|1, 0, g\rangle + C_{0,1,g}|0, 1, g\rangle \\
 & + C_{0,0,e}|0, 0, e\rangle + C_{2,0,g}|2, 0, g\rangle + C_{0,2,g}|0, 2, g\rangle \\
 & + C_{1,1,g}|1, 1, g\rangle + C_{1,0,e}|1, 0, e\rangle + C_{0,1,e}|0, 1, e\rangle,
 \end{aligned} \tag{9}$$

where  $|n, m, j\rangle = |n\rangle \otimes |m\rangle \otimes |j\rangle$  denotes a state with  $n$  photons in the cavity mode,  $m$  excitations in the NP mode, and the QE in the state of  $|j\rangle$  ( $j = e, g$ ). The coefficients  $C_{n,m,j}$  represent the probability amplitude of the corresponding state  $|n, m, j\rangle$ , for which the corresponding occupation probability is given by  $|C_{n,m,j}|^2$ . The equations of coefficients  $C_{n,m,j}$  varying with time can be obtained via the Schrödinger equation  $i\hbar\partial|\Psi(t)\rangle/\partial t = \hat{H}'_{\text{eff}}|\Psi(t)\rangle$  written for the non-Hermitian Hamiltonian

$$\begin{aligned}
 \hat{H}'_{\text{eff}} = & \hbar\left(\Delta_c - \frac{i\kappa_c}{2}\right)\hat{c}^\dagger\hat{c} + \hbar\left(\Delta_m - \frac{i\kappa_m}{2}\right)\hat{m}^\dagger\hat{m} \\
 & + \hbar\left(\Delta_e - \frac{i\gamma_s}{2}\right)\hat{\sigma}^\dagger\hat{\sigma} + i\hbar g_{me}(\hat{m}^\dagger\hat{\sigma} - \hat{m}\hat{\sigma}^\dagger) \\
 & + i\hbar g_{ce}(\hat{c}^\dagger\hat{\sigma} - \hat{c}\hat{\sigma}^\dagger) + \hbar g_{mc}(\hat{m}^\dagger\hat{c} + \hat{m}\hat{c}^\dagger) \\
 & - \hbar(\Omega_m\hat{m}^\dagger + \Omega_m^*\hat{m}) - \hbar\Omega_e(\hat{\sigma}^\dagger + \hat{\sigma}).
 \end{aligned} \tag{10}$$

Substituting the wave function of the system  $|\Psi(t)\rangle$  [Eq. (9)] and the effective non-Hermitian Hamiltonian  $\hat{H}'_{\text{eff}}$  [Eq. (10)] into the Schrödinger equation, a set of equations for the probability amplitude coefficients  $C_{n,m,j}$  can be given as

$$\begin{aligned}
 i\hbar\frac{\partial C_{1,0,g}}{\partial t} = & \hbar\left(\Delta_c - \frac{i\kappa_c}{2}\right)C_{1,0,g} + i\hbar g_{ce}C_{0,0,e} + \hbar g_{mc}C_{0,1,g} \\
 & - \hbar\Omega_m^*C_{1,1,g} - \hbar\Omega_eC_{1,0,e},
 \end{aligned} \tag{11}$$

$$\begin{aligned}
 i\hbar\frac{\partial C_{0,1,g}}{\partial t} = & \hbar\left(\Delta_m - \frac{i\kappa_m}{2}\right)C_{0,1,g} + i\hbar g_{me}C_{0,0,e} + \hbar g_{mc}C_{1,0,g} \\
 & - \hbar\Omega_mC_{0,0,g} - \sqrt{2}\hbar\Omega_m^*C_{0,2,g} - \hbar\Omega_eC_{0,1,e},
 \end{aligned} \tag{12}$$

$$\begin{aligned}
 i\hbar\frac{\partial C_{0,0,e}}{\partial t} = & \hbar\left(\Delta_e - \frac{i\gamma_s}{2}\right)C_{0,0,e} - i\hbar g_{me}C_{0,1,g} - i\hbar g_{ce}C_{1,0,g} \\
 & - \hbar\Omega_m^*C_{0,1,e} - \hbar\Omega_eC_{0,0,g},
 \end{aligned} \tag{13}$$

$$\begin{aligned}
 i\hbar\frac{\partial C_{2,0,g}}{\partial t} = & 2\hbar\left(\Delta_c - \frac{i\kappa_c}{2}\right)C_{2,0,g} + \sqrt{2}i\hbar g_{ce}C_{1,0,e} \\
 & + \sqrt{2}\hbar g_{mc}C_{1,1,g},
 \end{aligned} \tag{14}$$

$$\begin{aligned}
 i\hbar\frac{\partial C_{0,2,g}}{\partial t} = & 2\hbar\left(\Delta_m - \frac{i\kappa_m}{2}\right)C_{0,2,g} + \sqrt{2}i\hbar g_{me}C_{0,1,e} \\
 & + \sqrt{2}\hbar g_{mc}C_{1,1,g} - \sqrt{2}\hbar\Omega_mC_{0,1,g},
 \end{aligned} \tag{15}$$

$$\begin{aligned}
 i\hbar\frac{\partial C_{1,1,g}}{\partial t} = & \hbar\left(\Delta_c - \frac{i\kappa_c}{2}\right)C_{1,1,g} + \hbar\left(\Delta_m - \frac{i\kappa_m}{2}\right)C_{1,1,g} \\
 & + i\hbar g_{me}C_{1,0,e} + i\hbar g_{ce}C_{0,1,e} + \sqrt{2}\hbar g_{mc}C_{2,0,g} \\
 & + \sqrt{2}\hbar g_{mc}C_{0,2,g} - \hbar\Omega_mC_{1,0,g},
 \end{aligned} \tag{16}$$

$$\begin{aligned}
 i\hbar\frac{\partial C_{1,0,e}}{\partial t} = & \hbar\left(\Delta_c - \frac{i\kappa_c}{2}\right)C_{1,0,e} + \hbar\left(\Delta_e - \frac{i\gamma_s}{2}\right)C_{1,0,e} \\
 & - i\hbar g_{me}C_{1,1,g} - \sqrt{2}i\hbar g_{ce}C_{2,0,g} + \hbar g_{mc}C_{0,1,e} \\
 & - \hbar\Omega_eC_{1,0,g},
 \end{aligned} \tag{17}$$

$$\begin{aligned}
 i\hbar\frac{\partial C_{0,1,e}}{\partial t} = & \hbar\left(\Delta_m - \frac{i\kappa_m}{2}\right)C_{0,1,e} + \hbar\left(\Delta_e - \frac{i\gamma_s}{2}\right)C_{0,1,e} \\
 & - \sqrt{2}i\hbar g_{me}C_{0,2,g} - i\hbar g_{ce}C_{1,1,g} + \hbar g_{mc}C_{1,0,e} \\
 & - \hbar\Omega_mC_{0,0,e} - \hbar\Omega_eC_{0,1,g}.
 \end{aligned} \tag{18}$$

In the weak-driving scenario of interest, for the probability amplitude coefficients  $C_{n,m,j}$  we have the following relationship:  $C_{0,0,g} \gg \{C_{1,0,g}, C_{0,1,g}, C_{0,0,e}\} \gg \{C_{2,0,g}, C_{0,2,g}, C_{1,1,g}, C_{1,0,e}, C_{0,1,e}\}$ . The equations are solved for the steady state  $\partial C_{n,m,j}/\partial t = 0$ , then the equations for the coefficients  $C_{n,m,j}$  can be provided as

$$\begin{aligned}
 0 = & \left(\Delta_c - \frac{i\kappa_c}{2}\right)C_{1,0,g} + i g_{ce}C_{0,0,e} + g_{mc}C_{0,1,g} \\
 & - \Omega_m^*C_{1,1,g} - \Omega_eC_{1,0,e},
 \end{aligned} \tag{19}$$

$$\begin{aligned}
 0 = & \left(\Delta_m - \frac{i\kappa_m}{2}\right)C_{0,1,g} + i g_{me}C_{0,0,e} + g_{mc}C_{1,0,g} \\
 & - \Omega_mC_{0,0,g} - \sqrt{2}\Omega_m^*C_{0,2,g} - \Omega_eC_{0,1,e},
 \end{aligned} \tag{20}$$

$$\begin{aligned}
 0 = & \left(\Delta_e - \frac{i\gamma_s}{2}\right)C_{0,0,e} - i g_{me}C_{0,1,g} - i g_{ce}C_{1,0,g} \\
 & - \Omega_m^*C_{0,1,e} - \Omega_eC_{0,0,g},
 \end{aligned} \tag{21}$$

$$\begin{aligned}
 0 = & 2\left(\Delta_c - \frac{i\kappa_c}{2}\right)C_{2,0,g} + \sqrt{2}i g_{ce}C_{1,0,e} \\
 & + \sqrt{2}g_{mc}C_{1,1,g},
 \end{aligned} \tag{22}$$

$$\begin{aligned}
 0 = & 2\left(\Delta_m - \frac{i\kappa_m}{2}\right)C_{0,2,g} + \sqrt{2}i g_{me}C_{0,1,e} \\
 & + \sqrt{2}g_{mc}C_{1,1,g} - \sqrt{2}\Omega_mC_{0,1,g},
 \end{aligned} \tag{23}$$

$$\begin{aligned}
 0 = & \left(\Delta_c - \frac{i\kappa_c}{2}\right)C_{1,1,g} + \left(\Delta_m - \frac{i\kappa_m}{2}\right)C_{1,1,g} \\
 & + i g_{me}C_{1,0,e} + i g_{ce}C_{0,1,e} + \sqrt{2}g_{mc}C_{2,0,g} \\
 & + \sqrt{2}g_{mc}C_{0,2,g} - \Omega_mC_{1,0,g},
 \end{aligned} \tag{24}$$

$$\begin{aligned}
 0 = & \left(\Delta_c - \frac{i\kappa_c}{2}\right)C_{1,0,e} + \left(\Delta_e - \frac{i\gamma_s}{2}\right)C_{1,0,e} \\
 & - i g_{me}C_{1,1,g} - \sqrt{2}i g_{ce}C_{2,0,g} + g_{mc}C_{0,1,e} \\
 & - \Omega_eC_{1,0,g},
 \end{aligned} \tag{25}$$

$$\begin{aligned}
 0 = & \left(\Delta_m - \frac{i\kappa_m}{2}\right)C_{0,1,e} + \left(\Delta_e - \frac{i\gamma_s}{2}\right)C_{0,1,e} \\
 & - \sqrt{2}i g_{me}C_{0,2,g} - i g_{ce}C_{1,1,g} + g_{mc}C_{1,0,e} \\
 & - \Omega_mC_{0,0,e} - \Omega_eC_{0,1,g}.
 \end{aligned} \tag{26}$$

The coefficients  $C_{n,m,j}$  can be iteratively calculated by solving Eqs. (19)–(26) above. Under the weak-driving condition, the contributions from the higher states (i.e.,  $C_{2,0,g}$ ,  $C_{0,2,g}$ ,

$C_{1,1,g}$ ,  $C_{1,0,e}$ , and  $C_{0,1,e}$ ) to the steady-state values of  $C_{1,0,g}$ ,  $C_{0,1,g}$ , and  $C_{0,0,e}$  are negligible. So, the coefficients  $C_{1,0,g}$ ,  $C_{0,1,g}$ , and  $C_{0,0,e}$  of the single-excitation states can be found as

$$\begin{aligned} C_{1,0,g} &= \frac{g_{mc}(i\Omega_e g_{me} - \Omega_m \Delta'_e) - ig_{ce}(i\Omega_m g_{me} + \Omega_e \Delta'_m)}{M_1}, \\ C_{0,1,g} &= \frac{\Delta'_c(\Omega_m \Delta'_e - i\Omega_e g_{me}) + ig_{ce}(\Omega_e g_{mc} + i\Omega_m g_{ce})}{M_1}, \\ C_{0,0,e} &= \frac{\Delta'_c(\Omega_e \Delta'_m + i\Omega_m g_{me}) - g_{mc}(\Omega_e g_{mc} + i\Omega_m g_{ce})}{M_1}, \end{aligned} \quad (27)$$

with  $\Delta'_c = \Delta_c - i\kappa_c/2$ ,  $\Delta'_m = \Delta_m - i\kappa_m/2$ ,  $\Delta'_e = \Delta_e - i\gamma_s/2$ , and

$$M_1 = \begin{vmatrix} \Delta'_c & g_{mc} & ig_{ce} \\ g_{mc} & \Delta'_m & ig_{me} \\ -ig_{ce} & -ig_{me} & \Delta'_e \end{vmatrix}. \quad (28)$$

In the same manner, the coefficient  $C_{2,0,g}$  of the two-excitation state can be expressed as

$$\begin{aligned} C_{2,0,g} &= \frac{\alpha[g_{mc}(i\Omega_e g_{me} - \Omega_m \Delta'_e) - ig_{ce}(i\Omega_m g_{me} + \Omega_e \Delta'_m)] + \lambda[\Delta'_c(\Omega_m \Delta'_e - i\Omega_e g_{me}) + ig_{ce}(\Omega_e g_{mc} + i\Omega_m g_{ce})]}{M_1 M_2} \\ &\quad + \frac{\zeta[\Delta'_c(\Omega_e \Delta'_m + i\Omega_m g_{me}) - g_{mc}(\Omega_e g_{mc} + i\Omega_m g_{ce})]}{M_1 M_2}, \end{aligned} \quad (29)$$

where

$$M_2 = \begin{vmatrix} 2\Delta'_c & 0 & \sqrt{2}g_{mc} & \sqrt{2}ig_{ce} & 0 \\ 0 & 2\Delta'_m & \sqrt{2}g_{mc} & 0 & \sqrt{2}ig_{me} \\ \sqrt{2}g_{mc} & \sqrt{2}g_{mc} & \Delta'_c + \Delta'_m & ig_{me} & ig_{ce} \\ -\sqrt{2}ig_{ce} & 0 & -ig_{me} & \Delta'_c + \Delta'_e & g_{mc} \\ 0 & -\sqrt{2}ig_{me} & -ig_{ce} & g_{mc} & \Delta'_m + \Delta'_e \end{vmatrix}, \quad (30)$$

$$\begin{aligned} \alpha &= -ig_{ce}\Omega_e[\Delta'_m(\Delta'_c + \Delta'_m)(\Delta'_m + \Delta'_e) + 2g_{mc}g_{me}g_{ce} - g_{me}^2(\Delta'_c + \Delta'_m) - g_{ce}^2\Delta'_m - g_{mc}^2(\Delta'_m + \Delta'_e)] \\ &\quad - g_{ce}g_{me}[g_{me}^2\Omega_m - \Delta'_m\Omega_m(\Delta'_m + \Delta'_e)] + g_{ce}g_{mc}(g_{me}g_{mc}\Omega_m - g_{ce}\Delta'_m\Omega_m) \\ &\quad - g_{mc}\Delta'_m[\Omega_m(\Delta'_c + \Delta'_e)(\Delta'_m + \Delta'_e) + ig_{ce}g_{mc}\Omega_e - g_{mc}^2\Omega_m - ig_{me}\Omega_e(\Delta'_m + \Delta'_e)] \\ &\quad - ig_{mc}g_{me}[g_{me}^2\Omega_e + i\Omega_m g_{me}(\Delta'_c + \Delta'_e) - g_{me}^2\Omega_e], \end{aligned} \quad (31)$$

$$\begin{aligned} \lambda &= g_{mc}\Omega_m[g_{mc}(\Delta'_c + \Delta'_e)(\Delta'_m + \Delta'_e) + g_{mc}g_{me}^2 - g_{ce}g_{me}(\Delta'_c + \Delta'_e) - g_{mc}^3] \\ &\quad - g_{mc}\Delta'_m[ig_{me}g_{mc}\Omega_e - ig_{ce}\Omega_e(\Delta'_c + \Delta'_e)] - ig_{mc}^2g_{me}\Omega_e(\Delta'_c + \Delta'_e) \\ &\quad - g_{ce}g_{me}[\Omega_m g_{mc}(\Delta'_m + \Delta'_e) + i\Delta'_m g_{ce}\Omega_e - ig_{me}g_{mc}\Omega_e - g_{me}g_{ce}\Omega_m] \\ &\quad + ig_{ce}g_{mc}[\Delta'_m(\Delta'_c + \Delta'_m)\Omega_e - ig_{mc}g_{ce}\Omega_m - g_{mc}^2\Omega_e + ig_{me}\Omega_m(\Delta'_c + \Delta'_m)], \end{aligned} \quad (32)$$

and

$$\begin{aligned} \zeta &= -g_{mc}\Delta'_m[ig_{me}g_{mc}\Omega_m - ig_{ce}\Omega_m(\Delta'_c + \Delta'_e)] - ig_{mc}^2g_{me}\Omega_m(\Delta'_c + \Delta'_e) \\ &\quad - g_{ce}g_{me}[i\Delta'_m g_{ce}\Omega_m - ig_{me}g_{mc}\Omega_m] + ig_{ce}g_{mc}[\Delta'_m(\Delta'_c + \Delta'_m)\Omega_m - g_{mc}^2\Omega_m]. \end{aligned} \quad (33)$$

The other coefficients can also be solved using the same method, which are not shown for avoiding verbosity. Evidently, the analytical expressions of the physical quantities of concern can be approximately expressed in terms of these coefficients. In this regard, the average intracavity photon number and the second-order autocorrelation of the emitted photons from the cavity can be approximated to

$$\begin{aligned} n_c &= \langle \hat{c}^\dagger \hat{c} \rangle \\ &= |C_{1,0,g}|^2 + 2|C_{2,0,g}|^2 + |C_{1,1,g}|^2 + |C_{1,0,e}|^2 \\ &\simeq |C_{1,0,g}|^2, \end{aligned} \quad (34)$$

$$g_c^{(2)}(0) = \frac{\langle \hat{c}^\dagger \hat{c}^\dagger \hat{c} \hat{c} \rangle}{n_c^2} \simeq \frac{2|C_{2,0,g}|^2}{|C_{1,0,g}|^4}. \quad (35)$$

It is not difficult to find that, from the analytical expressions (27)–(33) together with Eqs. (34) and (35), the items linking to the statistical properties of photons are closely related to the size-dependent parameters such as the coupling strength  $g_{ce}$  between the QE and cavity mode, the coupling strength  $g_{me}$  between the NP and QE, and the coupling strength  $g_{mc}$  between the NP and cavity mode. The detail about the dependence of the tripartite coupling on the size-dependent system parameters is shown in Fig. 4 below. In the following, we will concentrate on the influence of these size-dependent structural parameters on the statistical properties of the NP-QE-cavity system.

It is important to mention that the intensity of the emitted light from the cavity is proportional to  $I_c = \kappa_c n_c$ . For brevity, in the discussion below we denote the intensity of



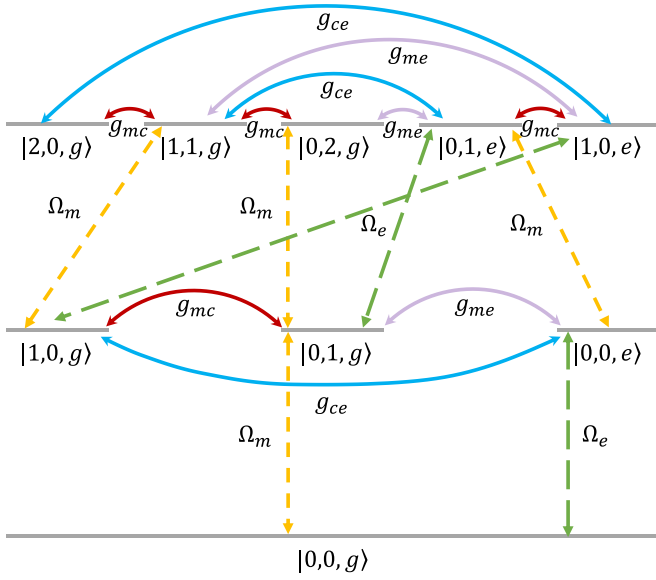


FIG. 2. Schematic diagram of the energy levels and excitation pathways of the coupled tripartite system corresponding to Fock states up to two photons. Energy diagram exhibiting the zero-, one-, and two-photon states (horizontal gray lines) and the transition pathways leading to the quantum interference in charge of the strong photon antibunching. States are marked as  $|n, m, j\rangle$ , where the first and second indices  $n$  and  $m$  in the ket correspond to the photon number in the cavity and NP modes, respectively, and the index  $j$  responsible for the excited state (ground state) of the two-level QE. The lilac double arrows represent the different energy-level transitions induced by the NP-QE coupling  $g_{me}$ . The blue double arrows indicate the different energy-level transitions caused by the QE-cavity coupling  $g_{ce}$ . The red double arrows mean the different energy-level transitions resulting from the NP-cavity coupling  $g_{mc}$ . The green double arrows denote the different energy-level transitions as a result of the coupling of the external driving laser with the two-level QE  $\Omega_e$ , while the yellow double arrows show the different energy-level transitions as a result of the coupling of the external driving laser with the NP  $\Omega_m$ .

the cavity emission light by  $n_c$  since they differ only by a constant coefficient  $\kappa_c$  which does not have any material impact on the results of concern. According to Eqs. (19)–(26), we display the schematic diagram of the energy levels and excitation pathways of the coupled system corresponding to the two-photon manifold, as shown in Fig. 2. From this figure, it is worth emphasizing that quantum interference can occur between different two-photon excitation pathways thanks to the introduction of the NP.

In the above approach, the system has been truncated, under the condition of weak driving, from infinite-dimensional Hilbert space to a two-photon excitation subspace spanned by nine basis states given in Eq. (9). If the higher-energy levels are excited, this approximation is no longer tenable. In order to prove the validity of the state expansion in the few photon subspace, we introduce a state-truncation fidelity defined as the sum of the occupying probabilities of the nine basis states in Eq. (9), i.e.,

$$F = |C_{0,0,g}|^2 + |C_{1,0,g}|^2 + |C_{0,1,g}|^2 + |C_{0,0,e}|^2 + |C_{2,0,g}|^2 + |C_{0,2,g}|^2 + |C_{1,1,g}|^2 + |C_{1,0,e}|^2 + |C_{0,1,e}|^2. \quad (36)$$

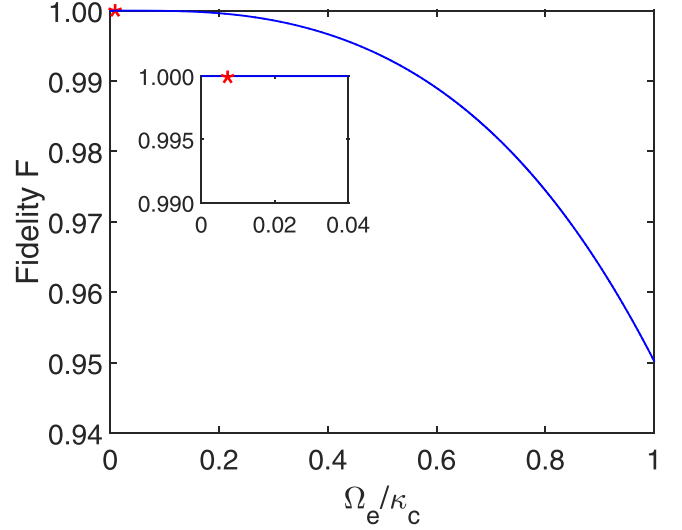


FIG. 3. State-truncation fidelity  $F$  defined by Eq. (36) as a function of the driving strength  $\Omega_e/\kappa_c$ . The inset shows a zoom-in view of the region marked by red star. Parameters used here are  $S_\alpha = 2$ ,  $\Delta_c = 0$ ,  $\omega_c = \omega_e = \omega_m = 2887.73$  meV,  $r_m = 5$  nm,  $d = 30$  nm,  $\theta = 0$ ,  $Q = 10^4$ , and  $\kappa_m = 53.28$  meV, respectively.

As described in Refs. [97,98], the introduction of fidelity  $F$  provides a powerful grasp to judge the effectiveness of the state truncation. More specifically, on the one hand, the fidelity  $F \approx 1$  not only illustrates that it is sufficient to describe the system using the few-photon excitation subspace spanned by the considered basis states, but also further ensures that the analytical results based on this approximation are valid. On the other hand, the fidelity  $F$  is much less than 1 ( $F \ll 1$ ), revealing that higher-photon excitation states are activated in this case, and thus it is insufficient to describe the system employing only these nine basis states in Eq. (9). To do so, in Fig. 3 we plot the fidelity  $F$  as a function of the driving-field strength  $\Omega_e/\kappa_c$  based directly on the full master equation (6). As clearly shown in Fig. 3, the fidelity  $F$  almost approaches 1 for a relatively weak driving-field strength  $\Omega_e/\kappa_c < 0.2$ . However, with the further increase of the driving-field strength, the fidelity  $F$  first drops slowly below unity, but still stays above 0.99 in the range of  $\Omega_e/\kappa_c \in [0.2, 0.58]$ , and then it decreases dramatically for a relatively strong driving-field strength  $\Omega_e/\kappa_c > 0.58$ . The excitation of multiphoton states under the condition of relatively strong driving-field strengths will deteriorate the fidelity  $F$  of the state truncation, which should be avoided to ensure the validity of the approximation for the state expansion described in Eq. (9). A red star in Fig. 3 is used to mark the position of the driving-field strength used in this work, thereby showing that it is located in the low-intensity regime and corresponds to the fidelity  $F = 1$ , which warrants the rationality of our state truncation used in the approximately analytical calculation.

The relationship between the tripartite coupling (i.e., the NP-QE coupling strength  $g_{me}$ , the NP-cavity coupling strength  $g_{mc}$ , and the QE-cavity coupling strength  $g_{ce}$ ) and the system parameters are presented in Fig. 4. It can be clearly seen that these coupling parameters are size or position dependent. For the purpose of more intuitively depicting them, the NP-QE

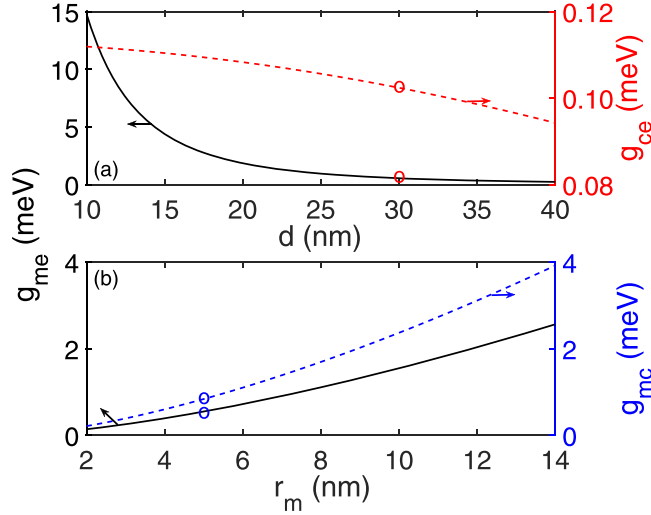


FIG. 4. Dependence of the tripartite coupling on the size-dependent system parameters. (a) The coupling strength  $g_{me}$  between the NP and QE (black solid line, left longitudinal axis) and the coupling strength  $g_{ce}$  between the QE and cavity (red dashed line, right longitudinal axis) as a function of the NP-to-QE distance  $d$  when  $r_m = 5$  nm. (b) The coupling strength  $g_{me}$  between the NP and QE (black solid line, left longitudinal axis) and the coupling strength  $g_{mc}$  between the NP and cavity (blue dashed line, right longitudinal axis) as a function of the NP radius  $r_m$  when  $d = 30$  nm. The open circles in (a) and (b) mark the values employed in the following calculations. In both cases, parameters used for calculations are  $S_\alpha = 2$ ,  $\omega_c = \omega_e = \omega_m = 2887.73$  meV,  $\theta = 0$ ,  $Q = 10^4$ ,  $\kappa_m = 53.28$  meV, and  $I_p = 1$  W/cm<sup>2</sup>, respectively.

coupling strength  $g_{me}$  and the QE-cavity coupling strength  $g_{ce}$  as a function of the NP-QE center-to-center distance  $d$  are plotted in Fig. 4(a). As shown in Fig. 4(a), both the coupling strength  $g_{me}$  and the coupling strength  $g_{ce}$  decrease monotonically with the increase of  $d$ . More specifically,  $g_{me}$  diminishes to a small value from 15 meV,  $g_{ce}$  decreases slightly, and the overall value of  $g_{ce}$  can ensure that the QE-cavity interaction is in the weak coupling region. As can be easily seen from Fig. 4(b), both the NP-QE coupling strength  $g_{me}$  and the NP-cavity coupling strength  $g_{mc}$  show a monotonically increasing trend with the increase of the NP radius  $r_m$ , which is apparent because  $g_{me}$  is proportional to the third-half power of  $r_m$ , i.e.,  $r_m^{3/2}$ , and  $g_{mc}$  is proportional to the third power of  $r_m$ , i.e.,  $r_m^3$ . It should be noted that the values of  $g_{me}$ ,  $g_{ce}$ , and  $g_{mc}$  are determined accordingly when a certain  $d$  or  $r_m$  is selected, and there are mutual constraints among three coupling parameters. By manipulating the NP-to-QE distance  $d$  and the NP radius  $r_m$ , the relative strengths of the local field can be modified, resulting in the adjustment of the tripartite coupling between the system components [99]. Therefore, engineering the NP-to-QE distance  $d$  and the NP radius  $r_m$  can be developed to tailor the coupling between the NP and QE, the interaction between the QE and cavity, and the coupling between the NP and cavity. Further contributions to the regulation of quantum statistical properties of the emitted (scattered) photons from the cavity (NP-QE molecule) will be discussed in great detail in Sec. V.

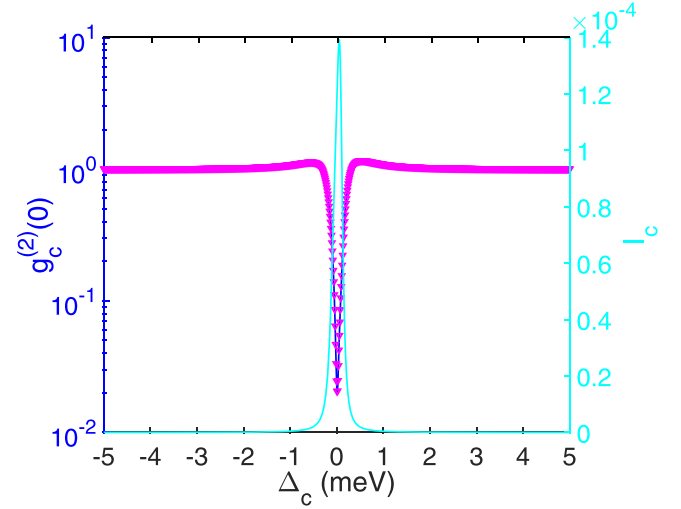


FIG. 5. Second-order autocorrelation function  $g_c^{(2)}(0)$  (left longitudinal axis) and intensity  $I_c$  (right longitudinal axis) of the cavity emission light as a function of the cavity-laser detuning  $\Delta_c$ . The blue solid line corresponds to the precise numerical solution, while the magenta triangle line corresponds to the analytical solution. Parameters used for calculations are  $S_\alpha = 2$ ,  $\omega_c = \omega_e = \omega_m = 2887.73$  meV,  $r_m = 5$  nm,  $d = 30$  nm,  $\theta = 0$ ,  $Q = 10^4$ ,  $\kappa_m = 53.28$  meV, and  $I_p = 1$  W/cm<sup>2</sup>, respectively. Other fixed parameters (not displayed) are given in the main text (cf. Sec. III).

## V. RESULTS AND DISCUSSIONS

In this section, we will focus on three correlation witnesses, namely, (i) the second-order autocorrelation of emitted photons from cavity, (ii) the second-order autocorrelation of scattered photons from NP-QE molecule, and (iii) the second-order cross correlation between both emitted and scattered photons. We show how the system parameters including geometric or material modification can be used to engineer the statistical properties of the radiation. First of all, we present both analytical and numerical results of the second-order autocorrelation function  $g_c^{(2)}(0)$  of the cavity emission photons for comparison and then we discuss the dependence of the photon statistics of the cavity emission photons on the system parameters in Sec. V A. Subsequently, how the size-related parameters (i.e., the NP-to-QE distance  $d$  and the NP radius  $r_m$ ) affect the second-order autocorrelation function  $g_p^{(2)}(0)$  of the NP-QE scattering photons is displayed in Sec. V B. Finally, the second-order cross-correlation function  $g_{cp}^{(2)}(0)$  between the cavity emission light and the NP-QE scattering light as a function of system parameters is considered in Sec. V C.

### A. Second-order autocorrelation of emitted photons from cavity

In order to compare the analytical solution (35) of the second-order autocorrelation function  $g_c^{(2)}(0)$  derived by the Schrödinger equation in the steady state with the numerical solution given by the master equation (6), we plot the second-order autocorrelation function  $g_c^{(2)}(0)$  versus the detuning  $\Delta_c$  between the resonance frequency  $\omega_c$  of the cavity mode and the frequency  $\omega_d$  of the driving laser field in Fig. 5 in which the blue solid line and the magenta triangle line denote the precise numerical solution and the analytical solution,

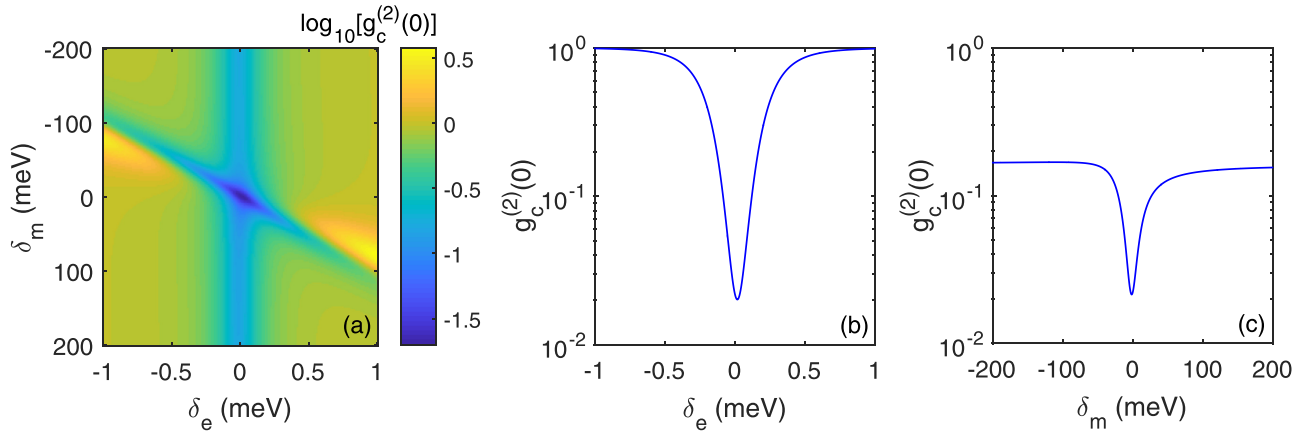


FIG. 6. (a) Logarithmic plot (of base 10) of the second-order autocorrelation function  $g_c^{(2)}(0)$  of the cavity emission photons versus the cavity-QE detuning  $\delta_e$  and the cavity-NP detuning  $\delta_m$ , where the color bar is on a logarithmic scale (of base 10). (b) Second-order autocorrelation function  $g_c^{(2)}(0)$  of the cavity emission photons as a function of the cavity-QE detuning  $\delta_e$  when  $\delta_m = 0$ . (c) Second-order autocorrelation function  $g_c^{(2)}(0)$  of the cavity emission photons as a function of the cavity-NP detuning  $\delta_m$  when  $\delta_e = 0$ . Parameters used for calculations are  $S_\alpha = 2$ ,  $\Delta_c = 0$ ,  $r_m = 5$  nm,  $d = 30$  nm,  $\theta = 0$ ,  $Q = 10^4$ ,  $\kappa_m = 53.28$  meV, and  $I_p = 1$  W/cm<sup>2</sup>, respectively.

respectively. It is revealed that the analytical solution obtained by the Schrödinger equation in the steady state can be faithfully reproduced by the full numerical solution obtained by the master equation.

Besides, we also display the intensity  $I_c$  of the cavity emission light varying with the cavity-laser detuning  $\Delta_c$  in Fig. 5. By looking at Fig. 5, we can see that the intensity of the emitted light from cavity follows the Lorentzian-type profile, and concurrently the strong antibunching signal can be detected near the maximum intensity. In this case, the system can be regarded as an effective single-photon blockade device, which not only plays a certain role in related measurement, but also has a guiding significance for practical experimental design to a certain extent.

In the analysis above, we consider the resonant cases for any two frequencies among the NP ( $\omega_m$ ), QE ( $\omega_e$ ), and cavity ( $\omega_c$ ), namely,  $\omega_m = \omega_e = \omega_c$ . We now turn to the situations where the NP, QE, and cavity are detuned from resonances. To do this, we define the detunings  $\delta_m = \omega_m - \omega_c$  and  $\delta_e = \omega_e - \omega_c$ , which lead to  $\delta_m - \delta_e = \omega_m - \omega_e$  among the NP, QE, and cavity. With these definitions at hand, from Eq. (5) we have the relations  $\Delta_m = \Delta_c + \delta_m$  and  $\Delta_e = \Delta_c + \delta_e$ . It is obvious that, when  $\delta_m = 0$  and  $\delta_e = 0$ , all three of the NP, QE, and cavity are resonant with each other. We then study how the statistical properties of the cavity emission photons are affected by both the cavity-QE detuning  $\delta_e$  and the cavity-NP detuning  $\delta_m$  by plotting a color two-dimensional (2D) map of the second-order autocorrelation function  $g_c^{(2)}(0)$  for the cavity emission photons in Fig. 6(a). It is found from this figure that the statistical properties of the cavity emission photons are sensitive to the cavity-QE detuning  $\delta_e$  and are robust to the cavity-NP detuning  $\delta_m$ , allowing one to optimize the antibunched photon generation by regulating the cavity-QE detuning  $\delta_e$  and the cavity-NP detuning  $\delta_m$ . Just to be more intuitive, Fig. 6(b) shows the second-order autocorrelation function  $g_c^{(2)}(0)$  as a function of the cavity-QE detuning  $\delta_e$  through choosing the cavity-NP detuning  $\delta_m = 0$  in Fig. 6(a). It can be seen from Fig. 6(b) that the antibunching effect of the cavity emission photons becomes more obvious when the

cavity is near resonance with the QE, and the minimum  $g_c^{(2)}(0)$  with the value of  $2.1 \times 10^{-2}$  occurs at  $\delta_e = 0$ . It conveys a message that the statistical properties of the cavity emission photons are sensitive to the cavity-QE detuning  $\delta_e$ , which can be optimized by tuning the detuning between the cavity and the QE using the method described in Sec. III. Figure 6(c) shows the cut of the second-order autocorrelation function  $g_c^{(2)}(0)$  along the cavity-QE detuning  $\delta_e = 0$  in Fig. 6(a), where the cavity-NP detuning  $\delta_m$  is varied. It is shown in Fig. 6(c) that the cavity emission photons can exhibit typical antibunching, i.e.,  $g_c^{(2)}(0) \ll 1$ , even if the NP-cavity detuning  $\delta_m$  changes on a large scale. This signifies an information that the statistical properties of the cavity emission photons are immune to the change of the NP-cavity detuning  $\delta_m$ , which makes the experimental realization of the scheme more friendly.

Now we explore how the NP can be exploited to control the statistical properties of the cavity emission photons. Recalling Sec. II, it is pointed out that the NP-QE coupling strength  $g_{me}$  and the QE-cavity coupling strength  $g_{ce}$  are position dependent, i.e.,  $g_{me} \propto 1/d^3$  and  $g_{ce} \propto \cos(2\pi d/\lambda_c)$ . In view of this, in Fig. 7 we plot the second-order autocorrelation function  $g_c^{(2)}(0)$  varying with the NP-to-QE distance  $d$  for the two different cases, i.e., with the NP (blue solid line) and without the NP (magenta dashed line). In the absence of the NP, the considered system is a typical single-QE-cavity QED system via driving the QE. Here, we consider the system under weak driving and weak QE-cavity coupling conditions. As demonstrated in Ref. [100], in the case of weak driving, the value of the second-order autocorrelation function is less than unity for small coupling strength because the high-order states cannot be excited by these weak-driving fields. As one can see in Fig. 7, with the introduction of the NP, the statistical properties of photons are well engineered under the weak-coupling condition, accompanied by either enhanced antibunching or a transition from strong antibunching to large bunching of the light and vice versa. In the vicinity of  $d = 18.83$  nm, the antibunching effect obtained in the two cases (i.e., with the NP and without the NP) is equivalent. Most notably, the influence

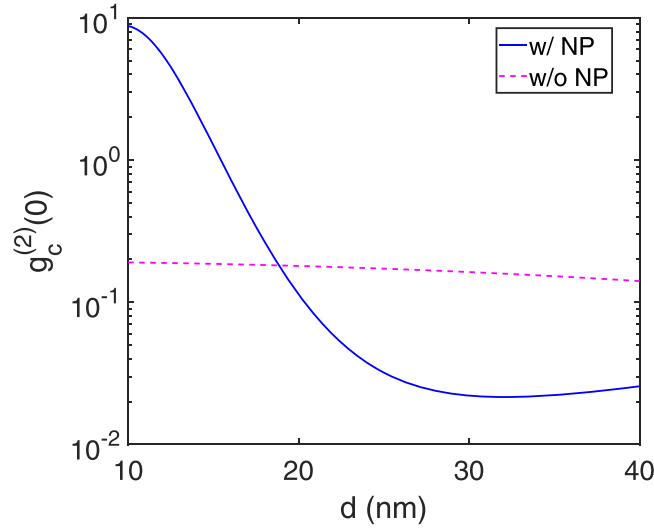


FIG. 7. Second-order autocorrelation function  $g_c^{(2)}(0)$  of the cavity emission light as functions of the NP-to-QE distance  $d$  with NP (blue solid line) and without NP (magenta dashed line). Parameters used for calculations are  $S_\alpha = 2$ ,  $\Delta_c = \delta_e = \delta_m = 0$ ,  $r_m = 5$  nm,  $\theta = 0$ ,  $Q = 10^4$ ,  $\kappa_m = 53.28$  meV, and  $I_p = 1$  W/cm<sup>2</sup>, respectively.

of the NP-to-QE distance  $d$  on the photon statistical properties shown in Fig. 7 reminds us how to manipulate the statistical properties of photons by changing  $d$ , that is, the NP and QE are set close to each other to obtain strong bunching or far away from each other to obtain strong antibunching. Therefore, selective photon statistics can be controlled at nanoscale.

The well-behaved sub-Poissonian character of the photons emitted by the cavity is due to the fact that the introduction of the NP adds a few additional transition pathways to the system. When the NP is absent, there exists only one transition pathway for the two-photon excitation and no quantum interference occurs for the atom-driven scheme [100]. However, as shown in Fig. 2, there exist several transition pathways to the two-photon excitation state  $|2, 0, g\rangle$  with the introduction of the NP, for example,  $|0, 0, g\rangle \xleftrightarrow{\Omega_m} |0, 1, g\rangle \xleftrightarrow{g_{mc}} |1, 0, g\rangle \xleftrightarrow{\Omega_m} |1, 1, g\rangle \xleftrightarrow{g_{mc}} |2, 0, g\rangle$  owing to the NP driven  $\Omega_m$  and the interaction  $g_{mc}$  between the NP and the cavity,  $|0, 0, g\rangle \xleftrightarrow{\Omega_e} |0, 0, e\rangle \xleftrightarrow{\Omega_m} |0, 1, e\rangle \xleftrightarrow{g_{mc}} |1, 0, e\rangle \xleftrightarrow{g_{ce}} |2, 0, g\rangle$ , caused by the NP driven  $\Omega_m$ , the QE driven  $\Omega_e$ , the interaction  $g_{mc}$  between the NP and the cavity, and the coupling  $g_{ce}$  between the QE and the cavity, etc. The destructive interference between different transition pathways makes the probability of two-photon excitation considerably decreasing, so that the probability of detecting state  $|2, 0, g\rangle$  approaches to zero. As a consequence, the photon blockade phenomenon induced by quantum interference can be realized, giving rise to the output of strongly antibunched photons.

In order to clearly show how the QE-cavity coupling strength  $g_{ce}$  affects the photon antibunching, the second-order autocorrelation function  $g_c^{(2)}(0)$  versus the coupling strength  $g_{ce}$  is plotted in Fig. 8 when the driving laser is tuned to resonance with the cavity mode frequency, i.e.,  $\Delta_c = 0$ . As shown in this figure, it is counterintuitive that the photon antibunching effect of the cavity does not increase monotonically

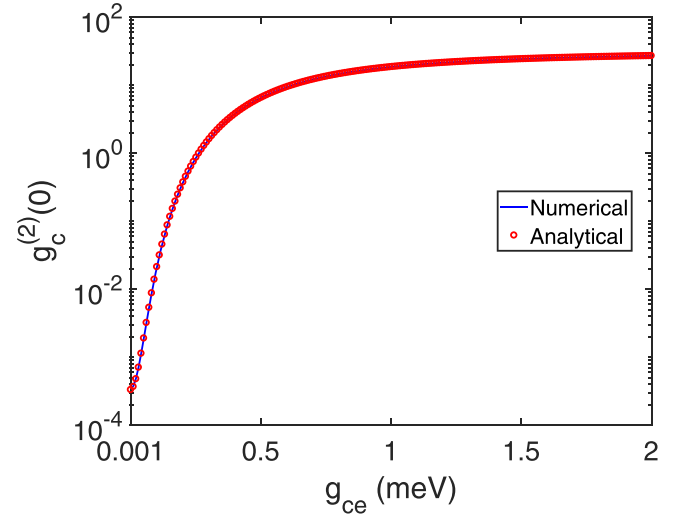


FIG. 8. Second-order autocorrelation function  $g_c^{(2)}(0)$  of the cavity emission light as a function of the coupling strength  $g_{ce}$  between the cavity mode and QE. Also shown in the plot is the comparison of the analytical prediction through Eq. (35) (the red open circles) with the numerical simulation obtained from Eqs. (6) and (7) (the blue solid line). Parameters used for calculations are  $S_\alpha = 2$ ,  $\Delta_c = \delta_e = \delta_m = 0$ ,  $r_m = 5$  nm,  $\theta = 0$ ,  $Q = 10^4$ ,  $\kappa_m = 53.28$  meV, and  $I_p = 1$  W/cm<sup>2</sup>, respectively.

with increasing  $g_{ce}$ , instead it is destroyed with the increase of  $g_{ce}$ . More specifically, under the condition of weak coupling, that is, the coupling strength  $g_{ce}$  is much smaller than the decay rate of the cavity ( $g_{ce} \ll \kappa_c$ ), the emitted photons from the cavity exhibit strong photon antibunching effect. When the coupling strength  $g_{ce}$  is comparable to the decay rate of the cavity, the cavity emission photons tend to be coherent. However, when further increasing  $g_{ce}$  to the strong-coupling region,  $g_c^{(2)}(0)$  increases and shows strong photon bunching effect. Thus, it conveys the information that the better photon antibunching corresponds to a smaller  $g_{ce}$ . In other words, strong photon antibunching effect can be realized under weak-coupling scenarios, which eliminate the requirement of strong nonlinearity that might not be easy to be achieved experimentally, and may have potential applications in the preparation of single-photon sources. Figure 8 also reveals that the results of both the numerical solution (blue solid line) and the analytical solution (red open circles) are in good agreement.

For illustrating how can we utilize the NP radius  $r_m$  to modify the photon statistical properties, we give the graph of the second-order autocorrelation function  $g_c^{(2)}(0)$  varying with  $r_m$  in Fig. 9. The result shows that the quantum statistics of the cavity emission photons can be manipulated on the nanoscale. Specifically, with the increase of  $r_m$ , the second-order autocorrelation function  $g_c^{(2)}(0)$  decreases initially until it reaches an antibunching minimum and then increases, corresponding to the photon statistics transforming from antibunching to bunching. Since the NP radius is closely related to the coupling between the NP and the cavity or the QE, featured in Fig. 4, the regulation of the cavity photon statistical properties by the NP radius  $r_m$  can be made.

To proceed further, a contour plot of the second-order autocorrelation function  $g_c^{(2)}(0)$  of the cavity emission

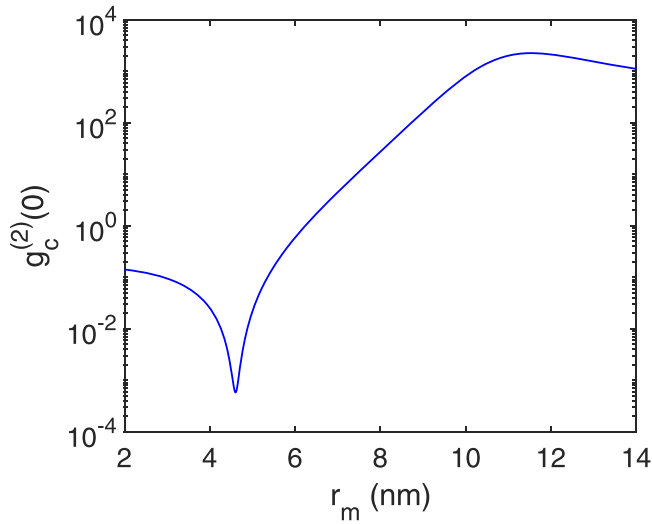


FIG. 9. Second-order autocorrelation function  $g_c^{(2)}(0)$  of the cavity emission light as functions of the NP radius  $r_m$ . Parameters used for calculations are  $S_\alpha = 2$ ,  $\Delta_c = \delta_e = \delta_m = 0$ ,  $d = 30$  nm,  $\theta = 0$ ,  $\kappa_m = 53.28$  meV,  $Q = 10^4$ , and  $I_p = 1$  W/cm<sup>2</sup>, respectively.

photons as a function of the NP-to-QE distance  $d$  and the NP radius  $r_m$  is displayed in Fig. 10 in order to clarify the size dependence of the statistical properties of the cavity emission photons. The color bar is on a logarithmic scale. Figure 10 clearly conveys a meaningful message: one can prepare the system for a sub-Poissonian statistics (see dark blue areas) or a super-Poissonian statistics (see dark red areas) by adjusting the NP-to-QE distance  $d$  or the NP radius  $r_m$ , which provides

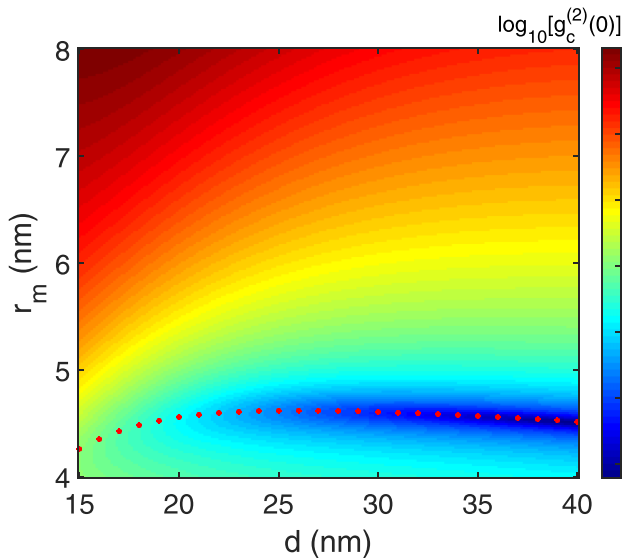


FIG. 10. Logarithmic plot (of base 10) of the second-order autocorrelation function  $g_c^{(2)}(0)$  of the cavity emission photons versus the NP-to-QE distance  $d$  and the NP radius  $r_m$ . The red dotted line represents the optimal antibunching condition derived by Eq. (29) analytically. Parameters used for calculations are  $S_\alpha = 2$ ,  $\Delta_c = \delta_e = \delta_m = 0$ ,  $\theta = 0$ ,  $Q = 10^4$ ,  $\kappa_m = 53.28$  meV, and  $I_p = 1$  W/cm<sup>2</sup>, respectively.

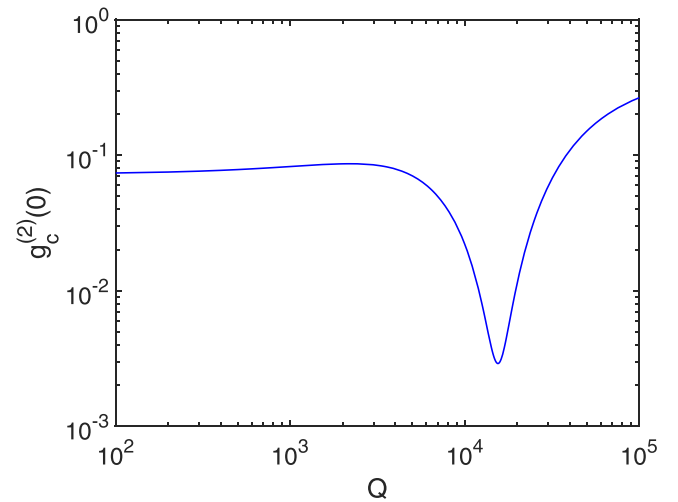


FIG. 11. Second-order autocorrelation function  $g_c^{(2)}(0)$  of the cavity emission light as a function of the cavity quality factor  $Q$ . Parameters used for calculations are  $S_\alpha = 2$ ,  $\Delta_c = \delta_e = \delta_m = 0$ ,  $r_m = 5$  nm,  $d = 30$  nm,  $\theta = 0$ ,  $\kappa_m = 53.28$  meV, and  $I_p = 1$  W/cm<sup>2</sup>, respectively.

us a way to control the single-photon blockade or alter it from strong antibunching to superbunching.

The optimal antibunching condition obtained by setting the analytical solution  $C_{2,0,g} = 0$  in Eq. (29) is highlighted in the figure (see the red dotted line), which coincides well with the full numerical solution. This further confirms that the underlying physical mechanism behind it is due to the quantum interference between distinct transition pathways as shown in Fig. 2. By adjusting the NP-to-QE distance  $d$  or the NP radius  $r_m$ , the NP-QE coupling strength  $g_{me}$ , the NP-cavity coupling strength  $g_{mc}$ , and the QE-cavity coupling strength  $g_{ce}$  alter accordingly (see Fig. 4). Under appropriate parameters, the occurrence of destructive quantum interference forbids the occupation of the two-excitation state  $|2, 0, g\rangle$ , thereby resulting in the generation of strong photon antibunching.

When the QE is placed in a cavity of resonance frequency  $\omega_c$  and decay rate  $\kappa_c$ , the corresponding quality factor  $Q$  is defined as the ratio of the cavity resonance frequency  $\omega_c$  to the corresponding decay rate  $\kappa_c$  (i.e.,  $Q = \omega_c/\kappa_c$ ), which reflects the degree of loss and measures the efficiency of energy storage [101]. In order to illustrate the influence of the cavity quality factor  $Q$  on the photon antibunching effect, we display in Fig. 11 the variation of the second-order autocorrelation function  $g_c^{(2)}(0)$  as a function of  $Q$ . As we all know, a low-quality factor is detrimental to achieving the strong-coupling regime. However, as depicted in Fig. 11, it is counterintuitive that the antibunching effect of the cavity emission photons does not decrease monotonically with increasing  $Q$ , instead it has a minimum at  $Q_{\text{opt}}$ . More specifically, the variation of  $g_c^{(2)}(0)$  with the quality factor  $Q$  exhibits a nonmonotonic behavior:  $g_c^{(2)}(0)$  decreases with increasing  $Q$  and arrives at the minimum (dip) around the optimal value of  $Q_{\text{opt}} = 1.56 \times 10^4$  where it corresponds to the minimum value of  $g_c^{(2)}(0) = 2.9 \times 10^{-3}$ . However, with further increasing of  $Q$ , the value of  $g_c^{(2)}(0)$  increases counterintuitively. It should be noted that using optical cavities with quality factors

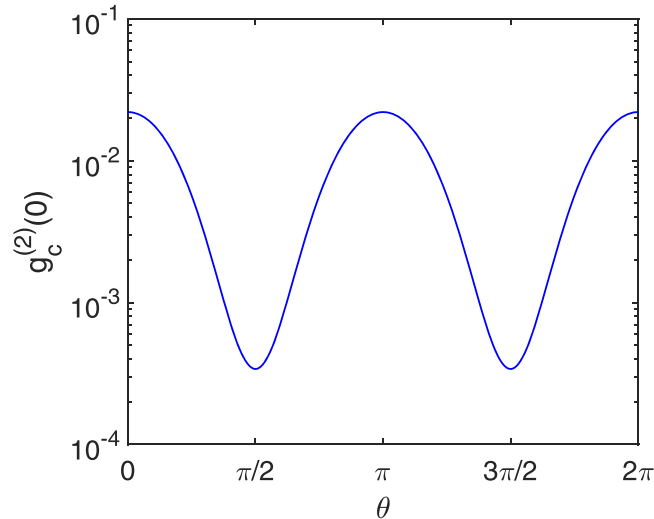


FIG. 12. Second-order autocorrelation function  $g_c^{(2)}(0)$  of the cavity emission light as a function of the relative orientation  $\theta$  between the dipole moment of the QE and the polarization vector of the cavity field. Parameters used for calculations are  $S_\alpha = 2$ ,  $\Delta_c = \delta_e = \delta_m = 0$ ,  $r_m = 5$  nm,  $d = 30$  nm,  $Q = 10^4$ ,  $\kappa_m = 53.28$  meV, and  $I_p = 1$  W/cm<sup>2</sup>, respectively.

even if on the order of 100 (which means in the bad cavity limit), the photon antibunching effect can also be observed in our system. Most strikingly, the statistical properties of the photons emitted from the cavity maintain antibunched in a wide range of parameters considered, which relaxes the difficulty of producing single-photon source in the experimental realization to a certain extent.

Again, in order to illustrate the influence of the polarization orientation on the statistical properties of the cavity emission photons, the second-order autocorrelation function  $g_c^{(2)}(0)$  versus the relative orientation  $\theta$  between the dipole moment of the QE and the polarization direction of the cavity field is plotted in Fig. 12. By looking at Fig. 12, we can observe that the second-order autocorrelation function  $g_c^{(2)}(0)$  shows  $\pi$ -periodic changes in the interval of  $\theta \in [0, 2\pi]$ . In addition, pronounced photon antibunching can be generated over the entire period of  $\pi$ . As we see,  $g_c^{(2)}(0)$  reaches a maximum value of  $2.2 \times 10^{-2}$  when the polarization direction of the cavity field is nearly perpendicular to that of the QE dipole moment (i.e.,  $\theta = N\pi$ ,  $N$  is an integer), while a minimum value of  $g_c^{(2)}(0) = 3.4 \times 10^{-4}$  appears when the polarization direction of the cavity field is nearly parallel to that of the QE dipole moment (i.e.,  $\theta = N\pi + \pi/2$ ), which implies that the degree of the nonclassical antibunching can be optimized by designing the proper polarization direction.

The dissipation channels of the NP dipolar mode include two decay processes: (1) radiative decay process which is due to a direct radiative decay route of the coherent electron oscillation into photons for larger particles and (2) nonradiative decay process which is caused by the creation of electron-hole pairs via either intraband excitations or interband transitions [44,50]. The silver NP used in our work is a much better plasmonic metal than some others, such as gold, characterized by its quality factor that reflects the period of surface

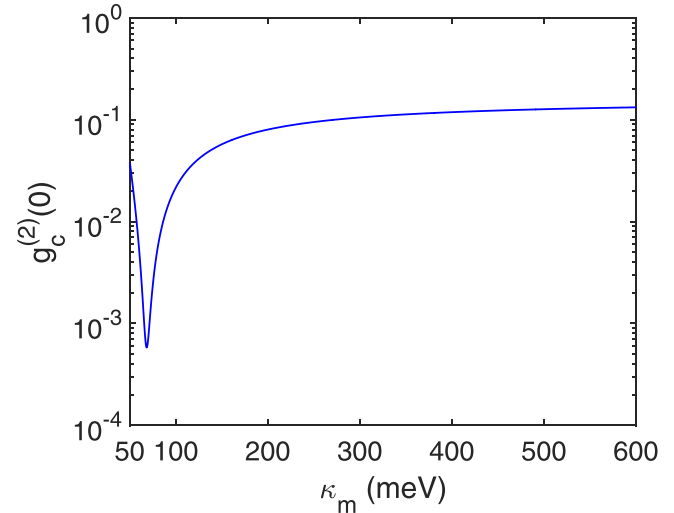


FIG. 13. Second-order autocorrelation function  $g_c^{(2)}(0)$  of the cavity emission light as a function of the damping  $\kappa_m$  of the NP. Parameters used for calculations are  $S_\alpha = 2$ ,  $\Delta_c = \delta_e = \delta_m = 0$ ,  $r_m = 5$  nm,  $d = 30$  nm,  $\theta = 0$ ,  $Q = 10^4$ , and  $I_p = 1$  W/cm<sup>2</sup>, respectively.

plasmon oscillation before field decays [59]. Typically, the quality factor of silver is several times that of gold, and thus the damping of silver chosen is quite optimistic. Considering a more general NP, the damping of the NP which is inversely proportional to the quality factor can even reach 10%–20% of the excitation energy [102–105]. Therefore, it is indisputable to discuss the influence of the NP loss on the statistical characteristics of the cavity emission photons. To this purpose, the second-order autocorrelation function  $g_c^{(2)}(0)$  as a function of the damping of the NP is depicted in Fig. 13. As can be seen, when increasing the damping of the NP gradually,  $g_c^{(2)}(0)$  decreases sharply at first, then increases rapidly after reaching the minimum value of  $5.8 \times 10^{-4}$  at  $\kappa_m = 68.17$  meV, and finally tends to arrive at a saturation value of 0.132. In particular, the entire damping region considered here displays strong nonclassical antibunching, i.e.,  $g_c^{(2)}(0) < 0.132$ , which manifests the robustness of the statistical properties of the cavity emission photons against the loss of the NP.

Since the measurements of the higher-order coherences provide a method to gain more in-depth understanding of the details of multiphoton emission, which can more clearly exhibit the nonclassical characteristics of the light source, we calculate the third-order autocorrelation function  $g_c^{(3)}(0)$  with the formula of  $g_c^{(3)}(0) = \langle (a^\dagger)^3 a^3 \rangle / \langle a^\dagger a \rangle^3$  for further studying the antibunching character of the cavity emission photons [106]. For comparison,  $g_c^{(2)}(0)$  and  $g_c^{(3)}(0)$  as a function of the cavity-laser detuning  $\Delta_c$  are plotted together in Fig. 14.  $g_c^{(2)}(0)$  is expected to contain information about the relative probability of two-photon emission and  $g_c^{(3)}(0)$  sustains information about the three-photon emission probability [107]. We can see that the values of  $g_c^{(3)}(0)$  are lower than those of  $g_c^{(2)}(0)$  [i.e.,  $g_c^{(3)}(0) < g_c^{(2)}(0) < 1$ ] in the photon antibunching regime of interest [97], which manifests that  $g_c^{(2)}(0)$  is mainly limited by two-photon events and not by higher-photon events [108].

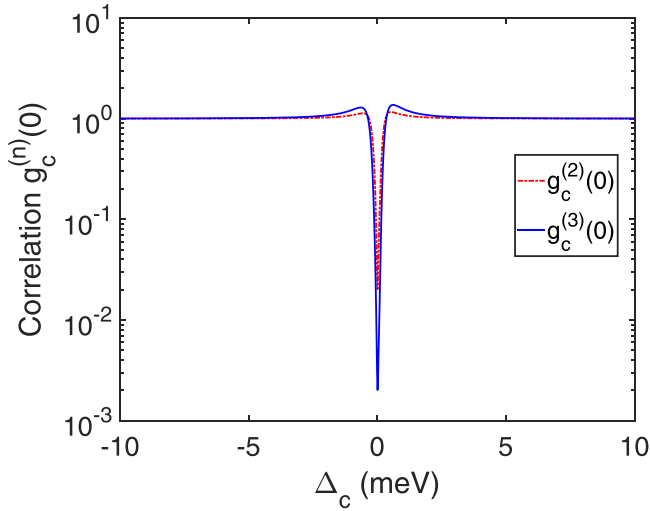


FIG. 14. Second- ( $n = 2$ ) and third-order ( $n = 3$ ) autocorrelation function  $g_c^{(2)}(0)$  (red dashed-dotted line) and  $g_c^{(3)}(0)$  (blue solid line) of the cavity emission light as a function of the cavity-laser detuning  $\Delta_c$ . Parameters used for calculations are  $S_\alpha = 2$ ,  $\delta_e = \delta_m = 0$ ,  $r_m = 5$  nm,  $d = 30$  nm,  $\theta = 0$ ,  $Q = 10^4$ ,  $\kappa_m = 53.28$  meV, and  $I_p = 1$  W/cm<sup>2</sup>, respectively.

### B. Second-order autocorrelation of scattered photons from NP-QE molecule

Under the excitation of an external driving laser, both the NP and QE scatter the incident light, and the total polarization operator can be constructed as  $\hat{p} = \chi^* \hat{m} + \mu \hat{o}$  according to [46,55,56]. The intensity of the scattered light from the NP-QE molecule is proportional to  $I_p = \langle \hat{p}^\dagger \hat{p} \rangle$  and the second-order autocorrelation function  $g_p^{(2)}(0)$  of the scattered light from the NP-QE molecule can be written as  $g_p^{(2)}(0) = \langle \hat{p}^{\dagger 2} \hat{p}^2 \rangle / I_p^2$  [46,109]. The formulations of  $I_p$  and  $g_p^{(2)}(0)$ , which are formally different but substantially equivalent to the above expressions, are presented in Refs. [50,54]. Figure 15 shows how the second-order autocorrelation function  $g_p^{(2)}(0)$  of the scattered light and the scattering intensity  $I_p$  vary with the cavity-laser detuning  $\Delta_c$ . As displayed in Fig. 15, the scattered light enters the region with antibunching by tuning the detuning in the range of  $(-2.37, 2.37)$  meV (pink shaded region). In this region, the statistical properties of the scattered photons from the NP-QE molecule show a high sensitivity to the detuning  $\Delta_c$ , which is reflected in the sharp change of the photon correlation shape line. The values of the second-order autocorrelation  $g_p^{(2)}(0)$  are altered by more than two orders of magnitude. This means that the photon statistics of the scattered light can be switched from bunching to antibunching by just tuning the cavity-laser detuning  $\Delta_c$ . At the same time, the peak of the scattering intensity is located in this region, bringing about the acquisition of the scattered photons from the NP-QE with strong antibunching and high scattering intensity.

Further below, a logarithmic plot (of base 10) of the second-order autocorrelation function  $g_p^{(2)}(0)$  of the NP-QE scattering photons as a function of the NP-to-QE distance  $d$  and the radius  $r_m$  of the NP is shown in Fig. 16. When the NP-to-QE distance  $d < 30$  nm, the statistical properties of

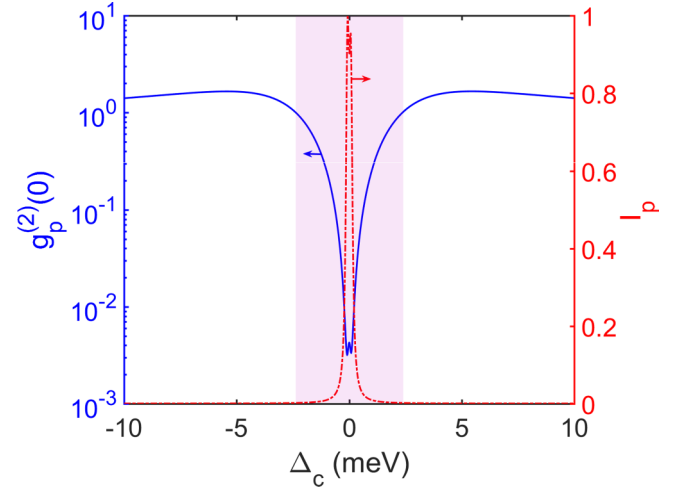


FIG. 15. Second-order autocorrelation function  $g_p^{(2)}(0)$  (blue solid line) and intensity (red dashed-dotted line) of the NP-QE scattering light as a function of the cavity-laser detuning  $\Delta_c$ . The red dashed-dotted line is normalized to the peak. The pink shaded region marks a high degree of antibunching and photon scattering. Parameters used for calculations are  $S_\alpha = 2$ ,  $\delta_e = \delta_m = 0$ ,  $r_m = 2$  nm,  $d = 30$  nm,  $\theta = 0$ ,  $Q = 10^4$ ,  $\kappa_m = 53.28$  meV, and  $I_p = 1$  W/cm<sup>2</sup>, respectively.

the NP-QE scattering photons gradually change from strong antibunching to bunching or even superbunching with the increase of the radius  $r_m$  of the NP. As the NP-to-QE distance in the area of  $d \in (30, 34)$  nm, a smooth transition of the statistics of the NP-QE scattering photons occurs from sub-Poissonian to Poissonian with the increase of the radius  $r_m$  of the NP. It is worth noting that the single-photon regime is usually characterized by  $g^{(2)}(0) < 0.5$  [37], which can be guaranteed in all selected radius ranges when the NP-to-QE

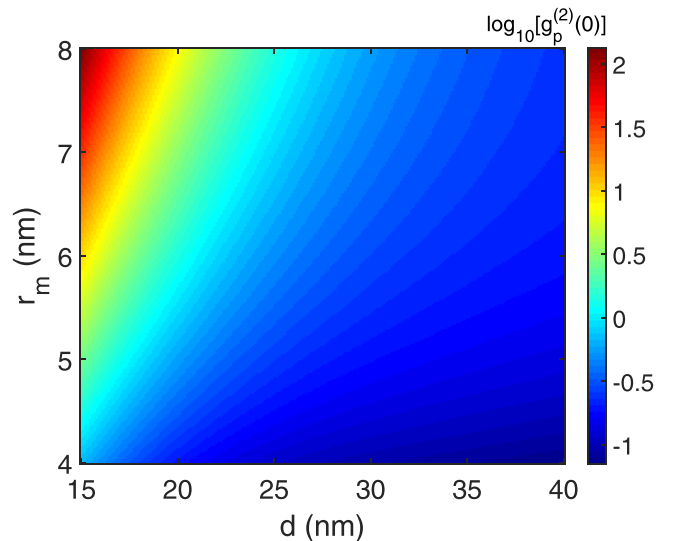


FIG. 16. Logarithmic plot (of base 10) of the second-order autocorrelation function  $g_p^{(2)}(0)$  of the NP-QE scattering photons as a function of the NP-to-QE distance  $d$  and the NP radius  $r_m$ . Parameters used for calculations are  $S_\alpha = 2$ ,  $\Delta_c = \delta_e = \delta_m = 0$ ,  $\theta = 0$ ,  $Q = 10^4$ ,  $\kappa_m = 53.28$  meV, and  $I_p = 1$  W/cm<sup>2</sup>, respectively.

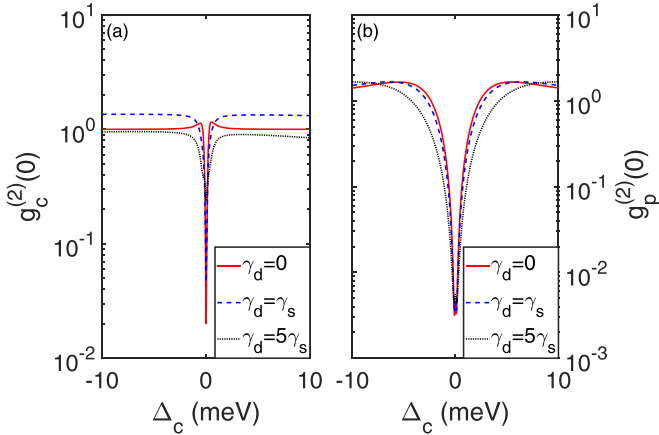


FIG. 17. (a) Second-order autocorrelation function  $g_c^{(2)}(0)$  of the cavity emission light and (b) second-order autocorrelation function  $g_p^{(2)}(0)$  of the NP-QE scattering light versus the cavity-laser detuning  $\Delta_c$  for the three different dephasing rates  $\gamma_d = 0$  (red solid line),  $\gamma_d = \gamma_s$  (blue dashed line), and  $\gamma_d = 5\gamma_s$  (black dotted line). Parameters used for calculations are  $S_\alpha = 2$ ,  $\delta_e = \delta_m = 0$ ,  $r_m = 5$  nm in (a) and  $r_m = 2$  nm in (b),  $d = 30$  nm,  $\theta = 0$ ,  $Q = 10^4$ ,  $\kappa_m = 53.28$  meV, and  $I_p = 1$  W/cm<sup>2</sup>, respectively.

distance  $d > 34$  nm. It can also be acquired from Fig. 16 that the farther the distance  $d$  is, the smaller the function  $g_p^{(2)}(0)$  is for a given NP radius  $r_m$ .

The influence of the pure dephasing effect was not considered in the previous discussion, in order to examine how the pure dephasing rate  $\gamma_d$  affects the statistical properties of photons emitted by the cavity and scattered by the NP-QE molecule in the system, the second-order autocorrelation function  $g_c^{(2)}(0)$  and  $g_p^{(2)}(0)$  varying with the cavity-laser detuning  $\Delta_c$  for various values of the dephasing rate  $\gamma_d$  are plotted in Fig. 17. Clearly, the dephasing effect has a detrimental effect on the realization of the photon blockade of the cavity field in Fig. 17(a), which reminds us that the dephasing rate should be minimized in practice. However, if the dephasing rate is close to the spontaneous emission rate, the quality of photon blockade can be guaranteed to a certain extent. The minimum values of the second-order autocorrelation function  $g_p^{(2)}(0)$  for the scattered photons from the NP-QE molecule vary slightly with the increase of  $\gamma_d$  from 0 to  $5\gamma_s$  in Fig. 17(b). What is more, the scattered photons with antibunching properties can be obtained in a wider range of detuning  $\Delta_c$  with the increase of  $\gamma_d$ , which illustrates the robustness of the statistical properties of the scattered photons to the dephasing rate.

### C. Second-order cross correlation between emitted and scattered photons

Figure 18 shows the second-order cross-correlation function  $g_{cp}^{(2)}(0)$  between the emitted photons from cavity and the scattered photons from NP-QE molecule varying with the cavity-laser detuning  $\Delta_c$ . It hints a strongly anticorrelated signal that the probability for the simultaneous presence of single photons in both modes is suppressed [17]. In other words, strong anticorrelation between the emitted photons and the scattered photons implies that single-photon emission can

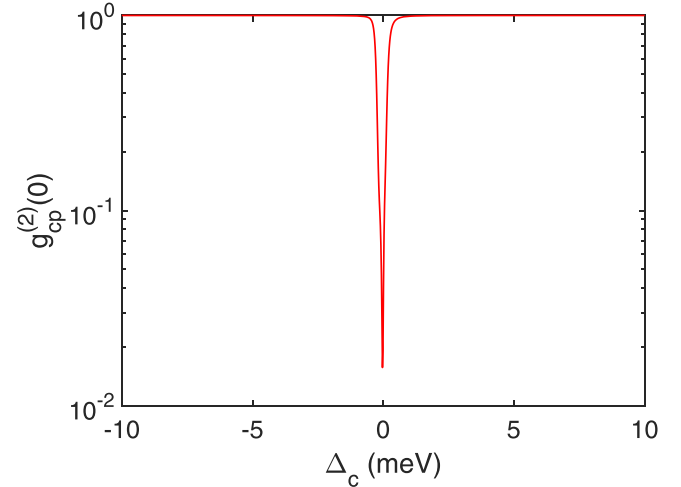


FIG. 18. Second-order cross-correlation function  $g_{cp}^{(2)}(0)$  between the cavity emission light and the NP-QE scattering light varying with the cavity-laser detuning  $\Delta_c$ . Parameters used for calculations are  $S_\alpha = 2$ ,  $\delta_e = \delta_m = 0$ ,  $r_m = 2$  nm,  $d = 30$  nm,  $\theta = 0$ ,  $Q = 10^4$ ,  $\kappa_m = 53.28$  meV, and  $I_p = 1$  W/cm<sup>2</sup>, respectively.

occur alternatively at the emitted photons from the cavity or the scattered photons from the NP-QE molecule in our system. The detection of a photon from one channel means that it is less likely that one will be found in the other.

Finally, a 2D map of the second-order cross-correlation function  $g_{cp}^{(2)}(0)$  (logarithmic scale) between the cavity emission photons and the NP-QE scattering photons as a function of the NP-to-QE distance  $d$  and the NP radius  $r_m$  is shown in Fig. 19. Looking closer, we find that strong correlation (see dark red areas) or anticorrelation (see dark blue areas)

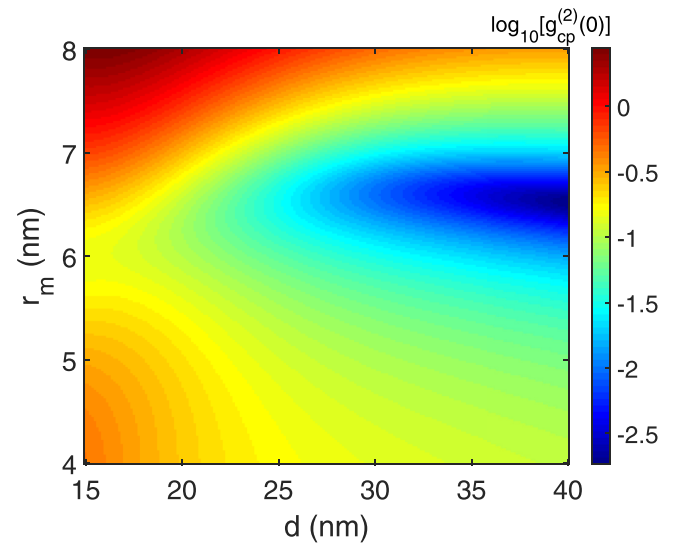


FIG. 19. Logarithmic plot (of base 10) of the second-order cross-correlation function  $g_{cp}^{(2)}(0)$  between the cavity emission and NP-QE scattering light as a function of the NP-to-QE distance  $d$  and the NP radius  $r_m$ . Parameters used for calculations are  $S_\alpha = 2$ ,  $\Delta_c = \delta_e = \delta_m = 0$ ,  $\theta = 0$ ,  $Q = 10^4$ ,  $\kappa_m = 53.28$  meV, and  $I_p = 1$  W/cm<sup>2</sup>, respectively.



between the cavity emission photons and the NP-QE scattering photons can be realized by manipulating the NP-to-QE distance  $d$  or the NP radius  $r_m$ . Rich photon statistical properties can be reflected in different parameter ranges. The common occurrence of photon blockade of the cavity emission photons (see Fig. 10) and photon blockade of the NP-QE scattering photons (see Fig. 16) in the same anticorrelated regime enables us to produce single-photon emission in the forms of cavity emission photons or NP-QE scattering photons alternatively. In addition, the cavity emission photon pairs and NP-QE scattering photon pairs can be generated in the same correlated regime (the generated cavity emission photons and the NP-QE scattering photons are correlated with each other), which can be applied to the two-photon gateway [110,111].

## VI. CONCLUSIONS

Summarizing, we have in detail explored the quantum statistical responses of photons in a fully coupled hybrid NP-QE-cavity system where a NP-QE molecule is placed into an optical cavity and all mutual couplings among them are considered. In such a configuration, using a combination of numerical and analytical methods, we assess the quantum correlation degree of the cavity emission photons and the NP-QE scattering photons by fixing our attention on, for example, (i) the second-order autocorrelation function  $g_c^{(2)}(0)$  of photons emitted by the cavity, (ii) the second-order autocorrelation function  $g_p^{(2)}(0)$  of photons scattered by the NP-QE molecule, and (iii) the second-order cross-correlation function  $g_{cp}^{(2)}(0)$  between the emitted photons by the cavity and the scattered photons by the NP-QE molecule in realistic parameter scenarios, respectively. With the introduction of the NP for tripartite interactions, the photon statistical properties of the fully coupled tripartite system can be well engineered in the weak-coupling regime, featuring the enhanced photon antibunching and the switching between strong antibunching and large bunching. The variation of the second-order autocorrelation function of the cavity emission light with the system parameters, e.g., the detuning between the cavity mode and driving laser, the distance between the NP and QE, and so on, shows the flexible tunability of photon statistics. Both strong antibunched photons with high intensity emitted from cavity and strong antibunched photons with high intensity scattered by hybrid NP-QE molecular can be captured in our tripartite system. We also find that the second-order cross-correlation function  $g_{cp}^{(2)}(0)$  clearly displays that not only the expected anticorrelated cavity emission and NP-QE scattering photons,

but also the cavity emission photon pairs, the NP-QE scattering photon pairs, as well as the correlated cavity emission and NP-QE scattering photons can be generated in different parameter regimes. On the other hand, it is revealed that the photon statistics of the cavity emission light shows a strong robustness for the quality factor of the cavity, manifesting with the maintenance of strong photon antibunching effect even at lower-quality factor. In addition, the photon statistics of the NP-QE scattering light is robust against the QE dephasing rate.

The tight link between the size-dependent parameters and the dipole response field of the NP enables it to modify the interplay between the system components. The combination of the external excitation and the coherent tripartite coupling is contributory to the destructive interference between different transition pathways for the two-photon excitation, promoting the occurrence of photon blockade. In this paper, we discuss the influence of various parameters on the photon statistical properties of the system. Among them, the size-dependent photon statistics are the ones we want to emphasize. Although the resonant case ( $\Delta_c = \delta_e = \delta_m = 0$ ), the smaller NP size [ $r_m \in (2, 6)$  nm], and the larger NP-to-QE distance [ $d \in (30, 40)$  nm] are the optimal conditions for obtaining photons with strong antibunching (the experimental feasibility of these conditions has been discussed in Sec. III), the more relaxed parameter requirements [e.g., the immunity to detuning (see Fig. 6 and the description about it) and the preservation of strong antibunching or bunching properties under a wide range of size-dependence parameters (see Figs. 10, 16, 19 and the descriptions about them)] also relieve the requirements of experimental conditions to a certain extent. In a nutshell, the small coupling strength required, the ease of parameter tuning, the relaxation of high-cavity quality factor, and the robustness to the QE dephasing rate promote the generation of single-photon sources, which is a crucial ingredient for various photonic quantum technologies ranging from quantum key distribution to optical quantum computing.

## ACKNOWLEDGMENTS

We would like to thank the two anonymous referees for their insightful and valuable comments. We also are grateful to X.-Y. Lü and R. Yu for enlightening discussions. The present research is supported in part by the National Key Research and Development Program of China under Contract No. 2021YFA1400700 and by the National Natural Science Foundation of China (NSFC) through Grant No. 11675058.

[1] J. L. O'Brien, A. Furusawa, and J. Vučković, Photonic quantum technologies, *Nat. Photonics* **3**, 687 (2009).  
 [2] E. M. Purcell, Spontaneous emission probabilities at radio frequencies, *Phys. Rev.* **69**, 681 (1946).  
 [3] B. Lounis and M. Orrit, Single-photon sources, *Rep. Prog. Phys.* **68**, 1129 (2005).  
 [4] B. Dayan, A. S. Parkins, T. Aoki, E. P. Ostby, K. J. Vahala, and H. J. Kimble, A photon turnstile dynamically regulated by one atom, *Science* **319**, 1062 (2008).

[5] A. Imamoğlu, H. Schmidt, G. Woods, and M. Deutsch, Strongly Interacting Photons in a Nonlinear Cavity, *Phys. Rev. Lett.* **79**, 1467 (1997).  
 [6] R. Huang, A. Miranowicz, J. Q. Liao, F. Nori, and H. Jing, Nonreciprocal Photon Blockade, *Phys. Rev. Lett.* **121**, 153601 (2018).  
 [7] E. Zubizarreta Casalengua, J. C. López Carreño, F. P. Laussy, and E. D. Valle, Conventional and unconventional photon statistics, *Laser Photonics Rev.* **14**, 1900279 (2020).

- [8] K. M. Birnbaum, A. Boca, R. Miller, A. D. Boozer, T. E. Northup, and H. J. Kimble, Photon blockade in an optical cavity with one trapped atom, *Nature (London)* **436**, 87 (2005).
- [9] A. Faraon, I. Fushman, D. Englund, N. Stoltz, P. Petroff, and J. Vučković, Coherent generation of non-classical light on a chip via photon-induced tunnelling and blockade, *Nat. Phys.* **4**, 859 (2008).
- [10] A. Reinhard, T. Volz, M. Winger, A. Badolato, K. J. Hennessy, E. L. Hu, and A. Imamoglu, Strongly correlated photons on a chip, *Nat. Photonics* **6**, 93 (2011).
- [11] W. W. Deng, G. X. Li, and H. Qin, Enhancement of the two-photon blockade in a strong-coupling qubit-cavity system, *Phys. Rev. A* **91**, 043831 (2015).
- [12] Y. X. Liu, X. W. Xu, A. Miranowicz, and F. Nori, From blockade to transparency: Controllable photon transmission through a circuit-QED system, *Phys. Rev. A* **89**, 043818 (2014).
- [13] A. J. Hoffman, S. J. Srinivasan, S. Schmidt, L. Spietz, J. Aumentado, H. E. Türeci, and A. A. Houck, Dispersive Photon Blockade in a Superconducting Circuit, *Phys. Rev. Lett.* **107**, 053602 (2011).
- [14] P. Rabl, Photon Blockade Effect in Optomechanical Systems, *Phys. Rev. Lett.* **107**, 063601 (2011).
- [15] J. Q. Liao and F. Nori, Photon blockade in quadratically coupled optomechanical systems, *Phys. Rev. A* **88**, 023853 (2013).
- [16] X. W. Xu, Y. J. Li, and Y. X. Liu, Photon-induced tunneling in optomechanical systems, *Phys. Rev. A* **87**, 025803 (2013).
- [17] A. Majumdar and D. Gerace, Single-photon blockade in doubly resonant nanocavities with second-order nonlinearity, *Phys. Rev. B* **87**, 235319 (2013).
- [18] H. Z. Shen, Y. H. Zhou, and X. X. Yi, Quantum optical diode with semiconductor microcavities, *Phys. Rev. A* **90**, 023849 (2014).
- [19] I. I. Smolyaninov, A. V. Zayats, A. Gungor, and C. C. Davis, Single-Photon Tunneling via Localized Surface Plasmons, *Phys. Rev. Lett.* **88**, 187402 (2002).
- [20] Y. L. Liu, G. Z. Wang, Y. X. Liu, and F. Nori, Mode coupling and photon antibunching in a bimodal cavity containing a dipole quantum emitter, *Phys. Rev. A* **93**, 013856 (2016).
- [21] T. C. H. Liew and V. Savona, Single Photons from Coupled Quantum Modes, *Phys. Rev. Lett.* **104**, 183601 (2010).
- [22] M. Bamba, A. Imamoglu, I. Carusotto, and C. Ciuti, Origin of strong photon antibunching in weakly nonlinear photonic molecules, *Phys. Rev. A* **83**, 021802(R) (2011).
- [23] A. Majumdar, M. Bajcsy, A. Rundquist, and J. Vučković, Loss-Enabled Sub-Poissonian Light Generation in a Bimodal Nanocavity, *Phys. Rev. Lett.* **108**, 183601 (2012).
- [24] J. Tang, W. D. Geng, and X. L. Xu, Quantum interference induced photon blockade in a coupled single quantum dot-cavity system, *Sci. Rep.* **5**, 9252 (2015).
- [25] J. P. Xu, S. L. Chang, Y. P. Yang, S. Y. Zhu, and G. S. Agarwal, Hyperradiance accompanied by nonclassicality, *Phys. Rev. A* **96**, 013839 (2017).
- [26] H. J. Snijders, J. A. Frey, J. Norman, H. Flayac, V. Savona, A. C. Gossard, J. E. Bowers, M. P. van Exter, D. Bouwmeester, and W. Löffler, Observation of the Unconventional Photon Blockade, *Phys. Rev. Lett.* **121**, 043601 (2018).
- [27] C. Vaneph, A. Morvan, G. Aiello, M. Féchant, M. Aprili, J. Gabelli, and J. Estève, Observation of the Unconventional Photon Blockade Effect in the Microwave Domain, *Phys. Rev. Lett.* **121**, 043602 (2018).
- [28] A. Miranowicz, J. Bajer, N. Lambert, Y. X. Liu, and F. Nori, Tunable multiphonon blockade in coupled nanomechanical resonators, *Phys. Rev. A* **93**, 013808 (2016).
- [29] B. Sarma and A. K. Sarma, Unconventional photon blockade in three-mode optomechanics, *Phys. Rev. A* **98**, 013826 (2018).
- [30] G. L. Zhu, X. Y. Lü, L. L. Wan, T. S. Yin, Q. Bin, and Y. Wu, Controllable nonlinearity in a dual-coupling optomechanical system under a weak-coupling regime, *Phys. Rev. A* **97**, 033830 (2018).
- [31] H. Flayac and V. Savona, Input-output theory of the unconventional photon blockade, *Phys. Rev. A* **88**, 033836 (2013).
- [32] D. Gerace and V. Savona, Unconventional photon blockade in doubly resonant microcavities with second-order nonlinearity, *Phys. Rev. A* **89**, 031803(R) (2014).
- [33] X. W. Xu and Y. Li, Tunable photon statistics in weakly nonlinear photonic molecules, *Phys. Rev. A* **90**, 043822 (2014).
- [34] Y. H. Zhou, H. Z. Shen, and X. X. Yi, Unconventional photon blockade with second-order nonlinearity, *Phys. Rev. A* **92**, 023838 (2015).
- [35] H. Flayac, D. Gerace, and V. Savona, An all-silicon single photon source by unconventional photon blockade, *Sci. Rep.* **5**, 11223 (2015).
- [36] H. Flayac and V. Savona, Single photons from dissipation in coupled cavities, *Phys. Rev. A* **94**, 013815 (2016).
- [37] H. Flayac and V. Savona, Unconventional photon blockade, *Phys. Rev. A* **96**, 053810 (2017).
- [38] A. Huck and U. L. Andersen, Coupling single emitters to quantum plasmonic circuits, *Nanophotonics* **5**, 483 (2016).
- [39] T. Yoshie, A. Scherer, J. Hendrickson, G. Khitrova, H. M. Gibbs, G. Rupper, C. Ell, O. B. Shchekin, and D. G. Deppe, Vacuum Rabi splitting with a single quantum dot in a photonic crystal nanocavity, *Nature (London)* **432**, 200 (2004).
- [40] J. P. Reithmaier, G. Sek, A. Löffler, C. Hofmann, S. Kuhn, S. Reitzenstein, L. V. Keldysh, V. D. Kulakovskii, T. L. Reinecke, and A. Forchel, Strong coupling in a single quantum dot-semiconductor microcavity system, *Nature (London)* **432**, 197 (2004).
- [41] K. Vahala, Optical microcavities, *Nature (London)* **424**, 839 (2003).
- [42] J. H. Li, S. T. Shen, C. L. Ding, and Y. Wu, Magnetically induced optical transparency in a plasmon-exciton system, *Phys. Rev. A* **103**, 053706 (2021).
- [43] E. Hutter and J. H. Fendler, Exploitation of localized surface plasmon resonance, *Adv. Mater.* **16**, 1685 (2004).
- [44] S. A. Maier, *Plasmonics: Fundamentals and Applications* (Springer, New York, 2007).
- [45] A. I. Kuznetsov, A. E. Miroshnichenko, M. L. Brongersma, Y. S. Kivshar, and B. Luk'yanchuk, Optically resonant dielectric nanostructures, *Science* **354**, aag2472 (2016).
- [46] A. Ridolfo, O. Di Stefano, N. Fina, R. Saija, and S. Savasta, Quantum Plasmonics with Quantum Dot-Metal Nanoparticle Molecules: Influence of the Fano Effect on Photon Statistics, *Phys. Rev. Lett.* **105**, 263601 (2010).
- [47] F. Peyskens and D. Englund, Quantum photonics model for nonclassical light generation using integrated nanoplasmonic cavity-emitter systems, *Phys. Rev. A* **97**, 063844 (2018).

- [48] Y. J. Wang, H. Ye, Z. Y. Yu, Y. M. Liu, and W. B. Xu, Sub-Poissonian photon statistics in quantum dot-metal nanoparticles hybrid system with gain media, *Sci. Rep.* **9**, 10088 (2019).
- [49] H. M. Doleman, E. Verhagen, and A. F. Koenderink, Antenna-cavity hybrids: Matching polar opposites for purcell enhancements at any linewidth, *ACS Photonics* **3**, 1943 (2016).
- [50] P. Peng, Y. C. Liu, D. Xu, Q. T. Cao, G. Lu, Q. Gong, and Y. F. Xiao, Enhancing Coherent Light-Matter Interactions through Microcavity-Engineered Plasmonic Resonances, *Phys. Rev. Lett.* **119**, 233901 (2017).
- [51] B. Gurlek, V. Sandoghdar, and D. Martín-Cano, Manipulation of quenching in nanoantenna-emitter systems enabled by external detuned cavities: A path to enhance strong-coupling, *ACS Photonics* **5**, 456 (2018).
- [52] Y. W. Lu, J. F. Liu, Z. Y. Liao, and X. H. Wang, Plasmonic-photonic cavity for high-efficiency single-photon blockade, *Sci. China Phys. Mech. Astron.* **64**, 274212 (2021).
- [53] M. O. Scully and M. S. Zubairy, *Quantum Optics*, (Cambridge University Press, Cambridge, UK, 1997).
- [54] E. Waks and D. Sridharan, Cavity QED treatment of interactions between a metal nanoparticle and a dipole emitter, *Phys. Rev. A* **82**, 043845 (2010).
- [55] K. R. McEnery, M. S. Tame, S. A. Maier, and M. S. Kim, Tunable negative permeability in a quantum plasmonic metamaterial, *Phys. Rev. A* **89**, 013822 (2014).
- [56] H. Hapuarachchi, M. Premaratne, Q. L. Bao, W. L. Cheng, S. D. Gunapala, and G. P. Agrawal, Cavity QED analysis of an exciton-plasmon hybrid molecule via the generalized nonlocal optical response method, *Phys. Rev. B* **95**, 245419 (2017).
- [57] W. Zhang, A. O. Govorov, and G. W. Bryant, Semiconductor-Metal Nanoparticle Molecules: Hybrid Excitons and the Nonlinear Fano Effect, *Phys. Rev. Lett.* **97**, 146804 (2006).
- [58] W. Zhang and A. O. Govorov, Quantum theory of the nonlinear Fano effect in hybrid metal-semiconductor nanostructures: The case of strong nonlinearity, *Phys. Rev. B* **84**, 081405(R) (2011).
- [59] M. I. Stockman, Nanoplasmonics: Past, present, and glimpse into future, *Opt. Express* **19**, 22029 (2011).
- [60] K. L. Kelly, E. Coronado, L. L. Zhao, and G. C. Schatz, The optical properties of metal nanoparticles: The influence of size, shape, and dielectric environment, *J. Phys. Chem. B* **107**, 668 (2003).
- [61] D. Sarid and W. Challener, *Modern Introduction to Surface Plasmons: Theory, Mathematica Modeling, and Applications* (Cambridge University Press, New York, 2010), Chap. 9.
- [62] A. Mazzei, S. Götzinger, L. de S. Menezes, G. Zumofen, O. Benson, and V. Sandoghdar, Controlled Coupling of Counter-propagating Whispering-Gallery Modes by a Single Rayleigh Scatterer: A Classical Problem in a Quantum Optical Light, *Phys. Rev. Lett.* **99**, 173603 (2007).
- [63] D. Jackson, *Classical Electrodynamics* (Wiley, New York, 1999).
- [64] D. X. Zhao, Y. Gu, H. Y. Chen, J. J. Ren, T. C. Zhang, and Q. H. Gong, Quantum statistics control with a plasmonic nanocavity: Multimode-enhanced interferences, *Phys. Rev. A* **92**, 033836 (2015).
- [65] S. T. Shen, Z. M. Wu, J. H. Li, and Y. Wu, Insights into Fano-type resonance fluorescence from quantum-dot-metal-nanoparticle molecules with a squeezed vacuum, *Phys. Rev. A* **104**, 013717 (2021).
- [66] T. P. Rossi, T. Shegai, P. Erhart, and T. J. Antosiewicz, Strong plasmon-molecule coupling at the nanoscale revealed by first-principles modeling, *Nat. Commun.* **10**, 3336 (2019).
- [67] F. Benz, M. K. Schmidt, A. Dreismann, R. Chikkaraddy, Y. Zhang, A. Demetriadou, C. Carnegie, H. Ohadi, B. D. Nijs, R. Esteban, J. Aizpurua, and J. J. Baumberg, Single-molecule optomechanics in “picocavities”, *Science* **354**, 726 (2016).
- [68] V. Myroshnychenko, J. R. Fernández, I. P. Santos, A. M. Funston, C. Novo, P. Mulvaney, L. M. L. Marzán and F. J. G. D Abajo, Modelling the optical response of gold nanoparticles, *Chem. Soc. Rev.* **37**, 1792 (2008).
- [69] D. F. Walls and G. J. Milburn, *Quantum Optics* (Springer, New York, 2007).
- [70] Q.-ul-Ain Gulfam and Z. Ficek, Highly directional photon superbunching from a few-atom chain of emitters, *Phys. Rev. A* **98**, 063824 (2018).
- [71] A. Aboulfotouh, M. Fikry, M. Mohamed, M. Omar, H. Rady, and Y. Elbasha, Spectroscopic study of oscillator strength and radiative decay time of colloidal CdSe quantum dots, *Opt. Quantum Electron.* **50**, 115 (2018).
- [72] V. I. Klimov, A. A. Mikhailovsky, S. Xu, A. Malko, J. A. Hollingsworth, C. A. Leatherdale, H. J. Eisler, and M. G. Bawendi, Optical gain and stimulated emission in nanocrystal quantum dots, *Science* **290**, 314 (2000).
- [73] C. R. Kagan, E. Lifshitz, E. H. Sargent, and D. V. Talapin, Building devices from colloidal quantum dots, *Science* **353**, aac5523 (2016).
- [74] C. Murray, C. Kagan, and M. G. Bawendi, Synthesis and characterization of monodisperse nanocrystals and close-packed nanocrystal assemblies, *Annu. Rev. Mater. Sci.* **30**, 545 (2000).
- [75] K. Santhosh, O. Bitton, L. Chuntonov, and G. Haran, Vacuum Rabi splitting in a plasmonic cavity at the single quantum emitter limit, *Nat. Commun.* **7**, 11823 (2016).
- [76] H. Leng, B. Szychowski, M.-C. Daniel, and M. Pelton, Strong coupling and induced transparency at room temperature with single quantum dots and gap plasmons, *Nat. Commun.* **9**, 4012 (2018).
- [77] P. Nagpal, N. C. Lindquist, S. H. Oh, and D. J. Norris, Ultra-smooth patterned metals for plasmonics and metamaterials, *Science* **325**, 594 (2009).
- [78] N. R. Jana, L. Gearheart, and C. J. Murphy, Seed-mediated growth approach for shape-controlled synthesis of spheroidal and rod-like gold nanoparticles using a surfactant template, *Adv. Mater.* **13**, 1389 (2001).
- [79] L. E. Ocola, Nanoscale geometry assisted proximity effect correction for electron beam direct write nanolithography, *J. Vac. Sci. Technol. B* **27**, 2569 (2009).
- [80] T. Hartsfield, W. S. Chang, S. C. Yang, T. Ma, J. W. Shi, L. Y. Sun, G. Shvets, S. Link, and X. Q. Li, Single quantum dot controls a plasmonic cavity’s scattering and anisotropy, *Proc. Natl. Acad. Sci. USA* **112**, 12288 (2015).
- [81] D. Ratchford, F. Shafei, S. Kim, S. K. Gray, and X. Li, Manipulating coupling between a single semiconductor quantum dot and single gold nanoparticle, *Nano Lett.* **11**, 1049 (2011).
- [82] Y. Akahane, T. Asano, B. S. Song, and S. Noda, High-Q photonic nanocavity in a two-dimensional photonic crystal, *Nature (London)* **425**, 944 (2003).

- [83] B. S. Song, S. Noda, T. Asano, and Y. Akahane, Ultra-high-Q photonic double-heterostructure nanocavity, *Nat. Mater.* **4**, 207 (2005).
- [84] S. Mosor, J. Hendrickson, B. C. Richards, J. Sweet, G. Khitrova, H. M. Gibbs, T. Yoshie, A. Scherer, O. B. Shchekin, and D. G. Deppe, Scanning a photonic crystal slab nanocavity by condensation of xenon, *Appl. Phys. Lett.* **87**, 141105 (2005).
- [85] J. Vučković and Y. Yamamoto, Photonic crystal microcavities for cavity quantum electrodynamics with a single quantum dot, *Appl. Phys. Lett.* **82**, 2374 (2003).
- [86] S. Gupta and E. Waks, Spontaneous emission enhancement and saturable absorption of colloidal quantum dots coupled to photonic crystal cavity, *Opt. Express* **21**, 29612 (2013).
- [87] I. Fushman, D. Englund, and J. Vučković, Coupling of PbS quantum dots to photonic crystal cavities at room temperature, *Appl. Phys. Lett.* **87**, 241102 (2005).
- [88] J. Yang, J. Heo, T. Zhu, J. Xu, J. Topolancik, F. Vollmer, R. Ilic, and P. Bhattacharya, Enhanced photoluminescence from embedded PbSe colloidal quantum dots in silicon-based random photonic crystal microcavities, *Appl. Phys. Lett.* **92**, 261110 (2008).
- [89] M. S. Anderson, Nearfield surface enhanced spectroscopy using targeted nanoparticle deposition, *Appl. Phys. Lett.* **92**, 123101 (2008).
- [90] J. Merlein, M. Kahl, A. Zuschlag, A. Sell, A. Halm, J. Boneberg, P. Leiderer, A. Leitenstorfer, and R. Bratschitsch, Nanomechanical control of an optical antenna, *Nat. Photonics* **2**, 230 (2008).
- [91] A. Bek, R. Jansen, M. Ringler, S. Mayilo, T. A. Klar, and J. Feldmann, Fluorescence enhancement in hot spots of AFM-designed gold nanoparticle sandwich, *Nano Lett.* **8**, 485 (2008).
- [92] M. Barth, S. Schietinger, S. Fischer, J. Becker, N. Nüsse, T. Aichele, B. Löchel, C. Sönnichsen, and O. Benson, Nanoassembled plasmonic-photonic hybrid cavity for tailored light-matter coupling, *Nano Lett.* **10**, 891 (2010).
- [93] J. E. Fröch, S. Kim, C. Stewart, X. X. Xu, Z. Q. Du, M. Lockrey, M. Toth, and I. Aharonovich, Photonic nanobeam cavities with nanopockets for efficient integration of fluorescent nanoparticles, *Nano Lett.* **20**, 2784 (2020).
- [94] R. H. Brown and R. Q. Twiss, Correlation between Photons in two Coherent Beams of Light, *Nature (London)* **177**, 27 (1956).
- [95] T. Tanabe, M. Notomi, H. Taniyama, and E. Kuramochi, Dynamic Release of Trapped Light from an Ultrahigh-Q Nanocavity via Adiabatic Frequency Tuning, *Phys. Rev. Lett.* **102**, 043907 (2009).
- [96] P. Colman, P. Lunnemann, Y. Yu, and J. Mørk, Ultrafast Coherent Dynamics of a Photonic Crystal all-Optical Switch, *Phys. Rev. Lett.* **117**, 233901 (2016).
- [97] A. Miranowicz, M. Paprzycka, Y. X. Liu, J. Bajer, and F. Nori, Two-photon and three-photon blockades in driven nonlinear systems, *Phys. Rev. A* **87**, 023809 (2013).
- [98] T. S. Yin, Q. Bin, G. L. Zhu, G. R. Jin, and A. X. Chen, Phonon blockade in a hybrid system via the second-order magnetic gradient, *Phys. Rev. A* **100**, 063840 (2019).
- [99] R. D. Artuso and G. W. Bryant, Quantum dot-quantum dot interactions mediated by a metal nanoparticle: Towards a fully quantum model, *Phys. Rev. B* **87**, 125423 (2013).
- [100] K. Hou, C. J. Zhu, Y. P. Yang, and G. S. Agarwal, Interfering pathways for photon blockade in cavity QED with one and two qubits, *Phys. Rev. A* **100**, 063817 (2019).
- [101] O. Bittona, S. N. Gupta, and G. Haran, Quantum dot plasmonics: from weak to strong coupling, *Nanophotonics* **8**, 559 (2019).
- [102] C. Schäfer and G. Johansson, A Shortcut to Self-Consistent Light-Matter Interaction and Realistic Spectra from First-Principles, *Phys. Rev. Lett.* **128**, 156402 (2022).
- [103] Z. J. Yang, T. J. Antosiewicz, and T. Shegai, Role of material loss and mode volume of plasmonic nanocavities for strong plasmon-exciton interactions, *Opt. Express* **24**, 20373 (2016).
- [104] T. P. Rossi, P. Erhart, and M. Kuisma, Hot-carrier generation in plasmonic nanoparticles: The importance of atomic structure, *ACS Nano* **14**, 9963 (2020).
- [105] J. Fojt, T. P. Rossi, T. J. Antosiewicz, M. Kuisma, and P. Erhart, Dipolar coupling of nanoparticle-molecule assemblies: An efficient approach for studying strong coupling, *J. Chem. Phys.* **154**, 094109 (2021).
- [106] A. Rundquist, M. Bajcsy, A. Majumdar, T. Sarmiento, K. Fischer, K. G. Lagoudakis, S. Buckley, A. Y. Piggott, and J. Vučković, Nonclassical higher-order photon correlations with a quantum dot strongly coupled to a photonic-crystal nanocavity, *Phys. Rev. A* **90**, 023846 (2014).
- [107] M. J. Stevens, S. Glancy, S. W. Nam, and R. P. Mirin, Third-order antibunching from an imperfect single-photon source, *Opt. Express* **22**, 3244 (2014).
- [108] J. H. Li and Y. Wu, Quality of photon antibunching in two cavity-waveguide arrangements on a chip, *Phys. Rev. A* **98**, 053801 (2018).
- [109] D. X. Zhao, All-optical active control of photon correlations: Dressed-state-assisted quantum interference effects, *Phys. Rev. A* **98**, 033834 (2018).
- [110] A. Kubanek, A. Ourjoumtsev, I. Schuster, M. Koch, P. W. H. Pinkse, K. Murr, and G. Rempe, Two-Photon Gateway in One-Atom Cavity Quantum Electrodynamics, *Phys. Rev. Lett.* **101**, 203602 (2008).
- [111] X. W. Xu, H. Q. Shi, A. X. Chen, and Y. X. Liu, Cross-correlation between photons and phonons in quadratically coupled optomechanical systems, *Phys. Rev. A* **98**, 013821 (2018).